Journal of Materials Chemistry C

ROYAL SOCIETY OF CHEMISTRY

REVIEW

View Article Online
View Journal

Cite this: DOI: 10.1039/d5tc03797b

Minimizing barriers to efficient mechanoluminescence *via* polymer matrix integration

Ji Yeon Kim,†[a] Hong In Jeong,†[a] Sujoy Bandyopadhyay,[a] Samiran Morang,[b] Uttam Manna,[b] Dong-Won Kang [c] and Hyosung Choi *[a]

Mechanoluminescent solids are emerging as prime candidates for next-generation industrial and biomedical technologies, enabling effective light-based stress sensing without external power sources. However, directly transmitting stress into solid-state materials can be rather challenging, as it not only requires the application of high stress levels but also lowers the detection sensitivity, thereby limiting the practical utility of even high-performance mechanoluminescent materials. To use their performance to the limit, integrating polymer matrices that indirectly yet efficiently transmit stress to solids through interfacial triboelectric effects represents a groundbreaking strategy to impart morphological freedom, reduce the required mechanical stress, and maximize sensitivity. In this review, we comprehensively summarize the fundamental principles and mechanisms of ML composite systems, highlighting the synergistic roles of various polymers in improving mechanical compliance, luminescence efficiency, and device adaptability. Furthermore, we summarize various application cases enabled by these polymer-based ML composite systems, illustrating their potential in healthcare sensors, smart textiles, and biomedical platforms. Finally, by providing design guidelines for selecting and engineering suitable polymer matrices, this review establishes a blueprint for extending mechanoluminescent composites into broader application domains. These insights position polymer integration not merely as a supporting element but as a central strategy and roadmap for developing next-generation, high-efficiency, and adaptive ML platforms.

Received 23rd October 2025,
Accepted 2nd December 2025

DOI: 10.1039/d5tc03797b

rsc.li/materials-c

1. Introduction

Stress sensing underpins a wide range of modern industrial[1] and biomedical technologies,[2–4] spanning applications from consumer electronics and automotive systems to healthcare devices,[5] soft robotics,[6] and aerospace engineering.[7] To meet the diverse demands of these fields, next-generation stress sensors must offer flexibility, remote readability, multimodal responsiveness, and biocompatibility. These requirements have prompted the exploration of new material platforms capable of transducing mechanical stimuli into optical signals without external power sources.[8]

Following its first discovery as light emission generated by the fracture of a candy,[9] mechanoluminescence (ML) has drawn growing attention as a promising route for energy-free, stress-responsive light emission.[10] ML solids can be categorized depending on the type of host material and defect structure and the diverse mechanisms such as triboelectric-induced excitation, piezoelectric potential–driven carrier detrapping, or even direct fracture-induced charge separation.[11] Among these candidates, the persistent luminescence in elastic-ML solids arises primarily from carrier detrapping processes triggered by piezoelectric potentials generated through lattice distortion under mechanical loading.[12] In representative non-centrosymmetric phosphors such as $SrAl_2O_4$:Eu^{2+},Dy^{3+},[13] CaZnOS:Mn^{2+},[12,14] and ZnS:Cu,[15,16] this internal piezopotential facilitates the release and radiative recombination of trapped carriers, yielding recoverable light emission upon repeated deformation. Nevertheless, directly applying mechanical stress to microscopic ML solids to achieve sufficient lattice distortion is highly challenging; it requires large loads, produces weak brightness, and limits device morphology and sensitivity.[17] These intrinsic limitations underscore the need for strategies

[a] Department of Chemistry, Research Institute for Convergence of Basic Science and Research Institute for Natural Sciences, Hanyang University, Seoul, 04763, Republic of Korea. E-mail: hschoi202@hanyang.ac.kr
[b] Department of Chemistry, Indian Institute of Technology Guwahati, Assam, 781039, India
[c] School of Energy Systems Engineering, Chung-Ang University, Dongjak-Gu, Seoul, 06974, Republic of Korea
† These authors contributed equally.

that can amplify the mechano-to-photon conversion process without increasing the applied stress.

A paradigm shift occurred in 2013, when integrating a soft and elastic polydimethylsiloxane (PDMS) matrix with ZnS:Cu microparticles, which yielded unexpectedly strong ML.[18] It was shown that the polymer matrix has the potential to act not merely as a structural binder but as a functional medium that imparts mechanical flexibility and generates interfacial triboelectric fields at the polymer–phosphor boundary.[19] These triboelectric effects could serve as an important driving force for ML, inducing piezoelectric polarization within the phosphor lattice through a piezo-photonic coupling process, which in turn leads to band bending and carrier detrapping.[20] This unique effect originating from the polymer matrix thus converts mechanical stimuli into triboelectric potentials that more effectively drive piezoelectric polarization than direct mechanical loading, allowing efficient ML activation under significantly reduced stress.

Based on this concept, controlling the strength and distribution of the interfacial triboelectric field has emerged as a key strategy to modulate ML performance. Recent studies demonstrated that the triboelectric field can be tuned by engineering the surface charge polarity, dielectric constant, and elasticity of polymers, which collectively govern the piezoelectric response of embedded phosphors.[21] In particular, balancing interfacial pore formation with polymer elasticity has proven critical; excessive elasticity diminishes charge accumulation, while moderate elasticity combined with strong negative triboelectricity promotes robust charge trapping and intense emission.[5] Such design tunability has transformed polymer-based ML composites into morphologically adaptive platforms capable of conforming to complex geometries and dynamic motions, thereby enabling applications in self-powered tactile sensors, stretchable displays, soft robotic skins, and wearable healthcare monitors.[23,24]

In this review, we highlight how polymer integration has evolved from a passive mechanical support to a decisive factor governing interfacial charge dynamics and light generation efficiency in ML systems. We first revisit the various fundamental mechanisms and limitations of conventional ML solids,[11,25,26] with particular attention to identifying the intrinsic material properties that enable effective coupling with polymers. This is followed by an overview of the operating principles of polymer–ML hybrid systems, which exploit triboelectric and piezo-photonic interactions to overcome these intrinsic constraints. We then discuss recent advances in interface engineering and composite design for high-efficiency, flexible polymer–ML hybrid systems and conclude by proposing design guidelines for polymer selection and integration strategies to guide the development of next-generation ML-based stress-sensing devices across industrial and biomedical domains. This review establishes a unified framework for designing polymer-based ML platforms, paving the way toward self-powered and adaptive optoelectronic technologies.

2. Understanding the fundamental mechanisms of solid-state ML for applying ML platforms

The ML behavior observed in polymer-based platforms is fundamentally rooted in the carrier dynamics of typical solid-state phosphors under mechanical deformation. However, it is important to note that not all phosphors are intrinsically compatible with polymer integration. Because polymer matrices influence ML primarily through interfacial charge interactions, mechanical compliance, and field-driven carrier modulation, polymer integration becomes effective only when the phosphor possesses the underlying mechanisms capable of coupling with these polymer-derived effects.

To explore the principles of polymer-integrated ML systems, it is first essential to clarify how light generation occurs in solid-state ML materials, since conventional classifications are often ambiguous when extended to polymer-integrated systems. Traditionally, ML mechanisms have been categorized according to the mode of mechanical excitation, such as brittle fracture, plastic deformation, or elastic distortion, leading to classifications like fracto-, plastico-, and elastic-ML (Fig. 1a).[11,27]

However, in polymer-based ML platforms,[28] these conventional classifications have become less practical, as triboelectric-induced ML phenomena are commonly observed across materials previously categorized as elastico-, plastico-, or tribo-mechanoluminescent, making the boundaries between these classes increasingly ambiguous.[29,30] From this fact, we focus on the unifying fundamental ML process, carrier detrapping and radiative recombination driven by a mechanically induced local potential, whether originating from fracture, dislocation motion, or interfacial triboelectric fields.[31,32] As shown in Fig. 1a, mechanical deformation in any form inevitably induces polarization within the material, leading to the formation of local or interfacial charge potentials. This phenomenon is the key focus of our discussion. As presented in Fig. 1b–d, regardless of the type of external stimulus, the common effect originating from such charge polarization can be understood as band tilting, which governs carrier transport and radiative recombination behavior. Therefore, it becomes necessary to reinterpret and reorganize solid-state ML mechanisms from the perspective of field generation and carrier dynamics, providing a clearer framework for selecting and designing phosphors suitable for polymer-based ML platforms (Fig. 1e).

2.1. Fracto- and plastic-ML

As shown in Fig. 2, the earliest form of ML was observed from brittle fracture of crystals such as quartz, sugar, and alkali halides,[9] where instantaneous bond cleavage generated strong transient electric fields that accelerated free electrons based on the Langevin's model (Fig. 2a).[33,34] Although these early observations confirmed that mechanical energy could be directly converted into trap mediative-ML, the process was destructive

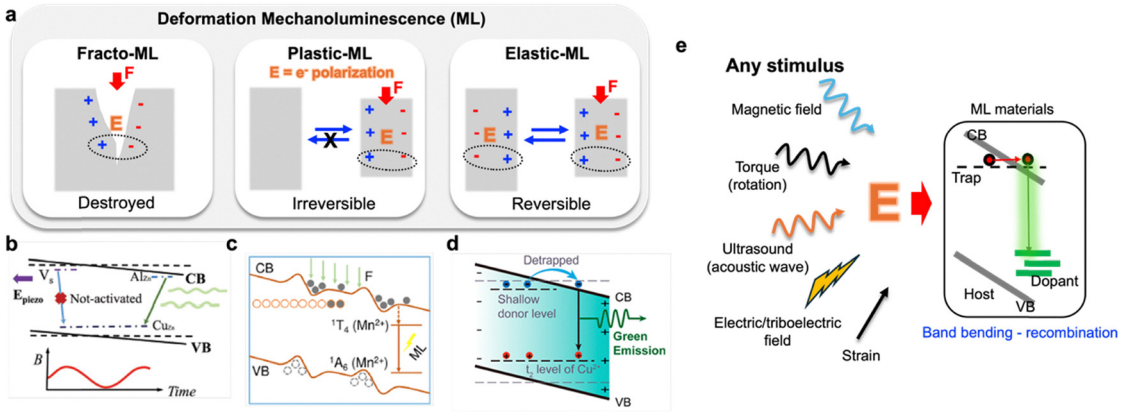

Fig. 1 (a) Classification of deformation ML. Band bending effect of ZnS:Cu for ML in previous several reports by means of the (b) magnetic field, (c) ultrasound, and (d) triboelectric effects. (e) The common effect of ML arising from electric field formation induced by charge polarization generated under external stimuli. Reproduced with permission from *Adv. Mater.*, 2017, **29**, 1701945. Copyright © 2017 Wiley-VCH GmbH. Reproduced with permission from *Nano Lett.*, 2025, **25**, 11747–11755. Copyright © 2025 American Chemical Society. Reproduced with permission from ACS *Appl. Mater. Interfaces*, 2022, **14**, 4775–4782. Copyright © 2022 American Chemical Society.

and non-repeatable, rendering it unsuitable for sensing or device applications (Fig. 2b).[35]

A milder form of ML occurs under plastic deformation, where dislocation motion and local bond rebuilding induce charge separation and electron transfer within the ZnS:Mn lattice (Fig. 2c).[36] This plastic deformation–induced field facilitates radiative recombination at Mn^{2+} centers, producing visible emission; however, irreversible defect migration during repeated strain leads to rapid luminescence fatigue and poor reproducibility (Fig. 2d). These regimes illustrate the fundamental limitation of direct mechanical excitation; most solid lattices cannot maintain strong localized electric fields without structural damage.

2.2. Trap-controlled ML

In many ML-active materials, including $SrAl_2O_4:Eu^{2+}$ and $CaZr(PO_4)_2:Eu^{2+}$, emission arises not from bond rupture but from the release of trapped carriers under mechanical stress.[27] Electrons in $SrAl_2O_4:Eu^{2+}$ photoexcited and stored in deep trap states (V_O) are released when mechanical stress or local strain perturbs the lattice potential, inducing transient internal electric fields that liberate trapped carriers (Fig. 3a).[37,38] This trap-controlled mechanism successfully explains the stress-dependent brightness in persistent ML phosphors but fails to account for the high emission efficiency and excellent reversibility observed in recent elastic ML platforms, where

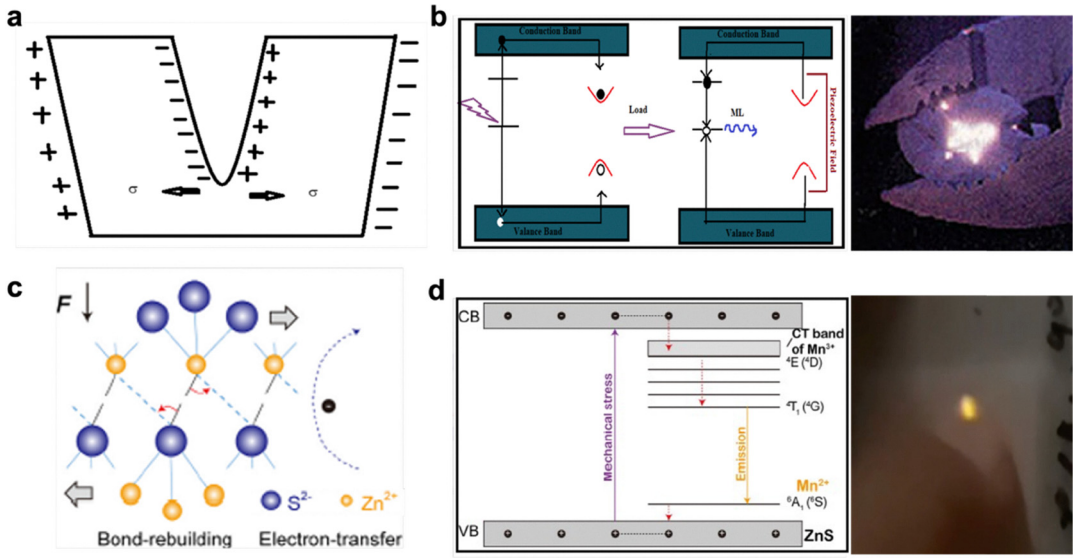

Fig. 2 (a) Langevin's model of fracto-ML. Reproduced with permission from *Acc. Mater. Res.*, 2021, **2**, 364. © The Authors, ACS Publications. (b) Schematic illustration of the fracto-ML mechanism. The inset shows the fracto-ML phenomenon observed from a candy under mechanical stress. Reproduced with permission from *J. Mater. Sci.: Mater. Electron.*, 2019, **30**, 19675. © Springer Nature. (c) Plastic deformation mechanism of ZnS:Mn, involving bond breaking/rebuilding and electron transfer under mechanical force. (d) Mechanism of plasticoluminescence in ZnS:Mn. The inset shows the ML emission of ZnS:Mn induced by scratching with a human finger. Reproduced with permission from *J. Lumin.*, 2021, **232**, 117838. © Elsevier B.V.

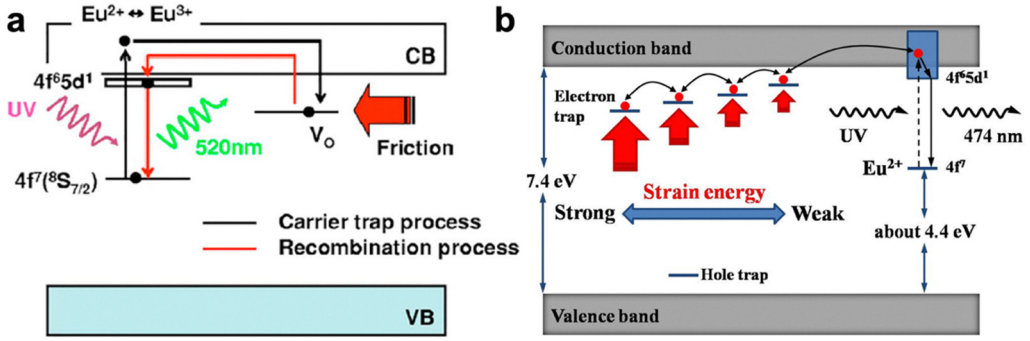

Fig. 3 Schematic illustration of the carrier-trap configurations and pathways responsible for ML. (a) Electron traps acting as the dominant carrier traps in $SrAl_2O_4:Eu^{2+}$. VB: valence band; CB: conduction band. Reproduced with permission from *J. Electrochem. Soc.* 2003, **150**, H75. © The Electrochemical Society. (b) Schematic diagram of the elastico-ML process in $CaZr(PO_4)_2:Eu^{2+}$. Reproduced with permission from *Opt. Express*, 2013, **21**, 13699. © Optica Publishing Group.

piezoelectric coupling facilitates stress-induced carrier detrapping and radiative recombination at Eu^{2+} in $CaZr(PO_4)_2:Eu^{2+}$ (Fig. 3b).[39] This discrepancy may suggests that an additional polarization mechanism, piezoelectric coupling, plays a crucial role in modulating carrier dynamics.

2.3. Piezoelectric-induced ML

In non-centrosymmetric lattices such as ZnS and CaZnOS, mechanical deformation generates a piezoelectric potential that serves as an internal driving field for carrier migration and detrapping (Fig. 4a).[40] The resulting band bending facilitates electron escape from traps and subsequent radiative recombination at dopant sites. This phenomenon, often referred to as piezo-phototronic coupling, demonstrates a direct correlation between lattice polarization and photon emission (Fig. 4b).[20] The piezoelectric effect enables high brightness and recoverable luminescence in rigid lattices by generating strong transient polarization under mechanical stress. However, this polarization dissipates rapidly once the stress is released. Therefore, achieving efficient and repeatable ML requires considering strategies that enhance the sensitivity of the piezoelectric effect and enable its sustained operation under repeated mechanical stimuli.

2.4. Elastic ML

Among the various ML mechanisms, elastic ML represents the most useful solid-state ML regime, where reversible light emission occurs entirely within the elastic deformation range. In this regime, lattice distortion induces internal piezoelectric polarization that modulates the band structure and lowers trap depths, enabling carrier detrapping and radiative recombination without permanent structural damage. As illustrated in Fig. 5, the elastic ML of ZnS:Mn originates from the synergistic interaction between stacking-fault-induced internal electric fields and externally applied piezoelectric polarization.[31] Fig. 5a schematically depicts how stacking faults within the wurtzite ZnS lattice act as charged interfaces that locally distort the potential landscape and create filled traps even under low mechanical stress. When a small external force (<10 MPa) is applied, these charged planes strongly enhance the local piezoelectric field, leading to band bending and charge separation across the stacking-fault interfaces (Fig. 5b). The amplified internal field then releases trapped carriers that recombine radiatively at Mn^{2+} luminescent centers, producing bright emission during elastic deformation (Fig. 5c). Upon stress release, the lattice fully recovers to its original configuration while the trap states are re-established, enabling reversible and repeatable luminescence (Fig. 5d).

Recently, a defect-localized ML model describing the elastic ML behavior was reported, in which Cu^+–S vacancy complexes in ZnS act as dynamic charge funnels that mediate carrier trapping and release. Density functional theory calculations (Fig. 5e and f) revealed that Cu^+–S vacancy (V_S) complexes in ZnS create localized internal electric fields and mid-gap states that narrow the effective band gap under elastic strain. When a small tensile strain (+2%) is applied, the valence-band maximum associated with the S vacancy and the conduction-band minimum of the ZnS lattice become energetically closer, facilitating indirect electronic transitions and enhancing the probability of radiative recombination even under minimal stress. The corresponding wave-function analysis confirmed that electrons localized at the S vacancy can be easily excited to the conduction band due to this band-gap reduction. Based on both computational and experimental findings, Fig. 5g schematically summarizes the defect-localized ML mechanism, in which local lattice distortion around Cu-related V_S sites modulates the band structure and drives elastic ML emission at $\approx$510 nm. These studies indicate that elastic ML provides the most practical and efficient regime among solid-state ML mechanisms, offering reversible operation and high emission stability.

2.5. Guiding principles for selecting solid-state phosphors in polymer-based ML platforms

From these mechanisms, we seek to understand a consistent physical picture, whether initiated by fracture, plastic slip, piezoelectric polarization, or defect-related fields, which serves as a crucial basis for determining whether a phosphor can be

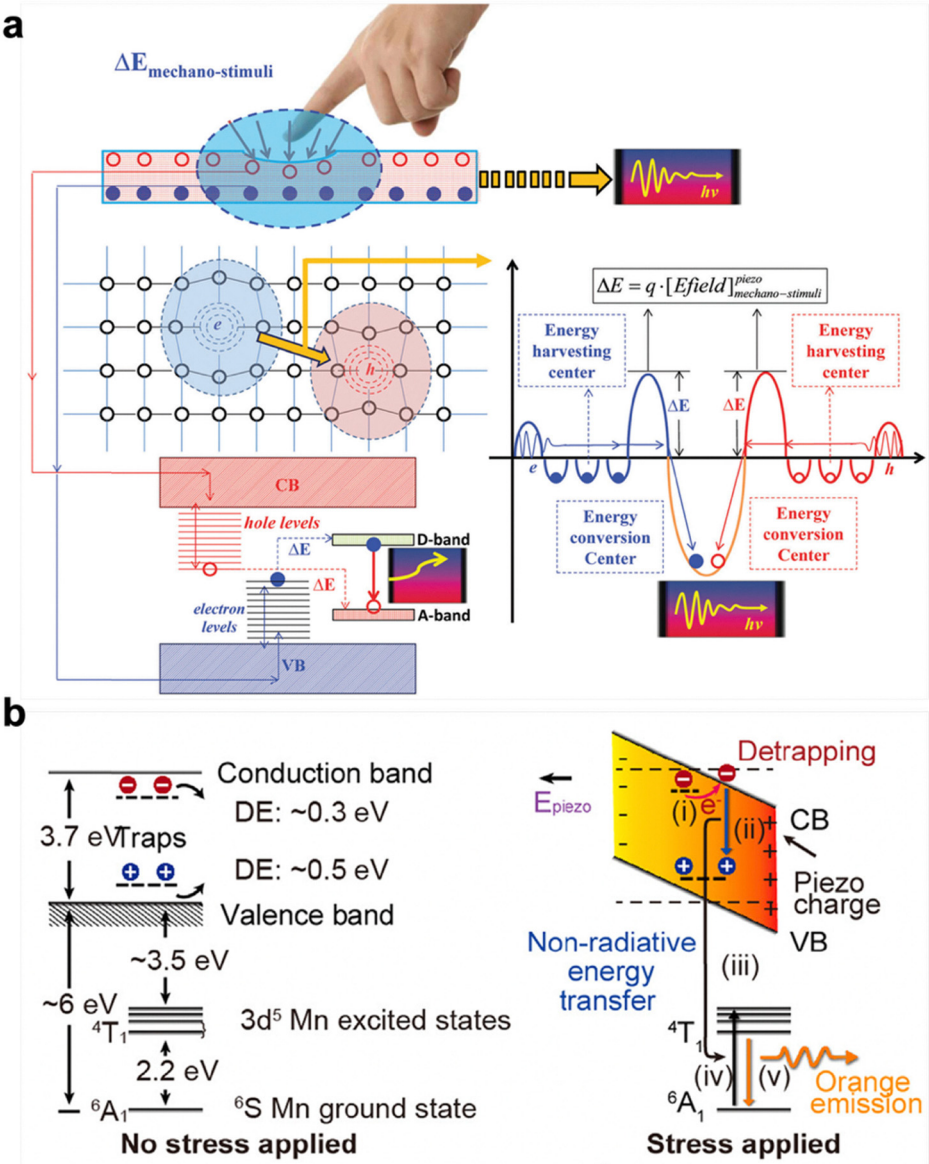

Fig. 4 (a) Schematic illustration of the native point defect–assisted energy conversion model describing upconverted mechano-persistent luminescence. Reproduced with permission from *Phys. Chem. Chem. Phys.* 2016, **18**, 25946. © The Royal Society of Chemistry. (b) Band diagram of Mn-doped ZnS showing the piezophotonic effect, in which a strain-induced piezopotential facilitates electron detrapping and radiative recombination during the ML process. Reproduced with permission from *Nano Energy* 2019, **55**, 389. © Elsevier B.V.

effectively integrated with a polymer matrix. We realized that all forms of mechanical stimuli inherently induce charge polarization or imbalance within the lattice, as well as charge separation at the surface (Fig. 1e). These induced potentials as a common driving force from mechanical energy modulate the band structure, release trapped carriers, and enable their radiative recombination at dopant centers (Fig. 6a).[19,41–44]

For example, a recent report provided valid evidence that luminescence can be triggered in ZnS-based and related phosphors not only by mechanical stress but also by external stimuli such as ultrasound, magnetic fields, or triboelectric potentials (Fig. 6b–f).[32] Therefore, in polymer-based ML platforms, conventional classifications may become somewhat ambiguous, and it is crucial to first recognize that interfacial triboelectric fields activate internal pathways, such as band bending, that facilitate carrier detrapping and subsequent radiative recombination.

This understanding provides critical insight into the selection criteria for solid-state phosphors applicable to polymer-based ML platforms, which are fundamentally based on interfacial triboelectric effects. To achieve efficient light generation under interfacial triboelectric fields, the material should either (i) allow surface charge separation capable of generating a bias-like potential under triboelectric excitation, or (ii) possess a reversible lattice structure that can be elastically distorted through inverse piezoelectric effects under an applied electric

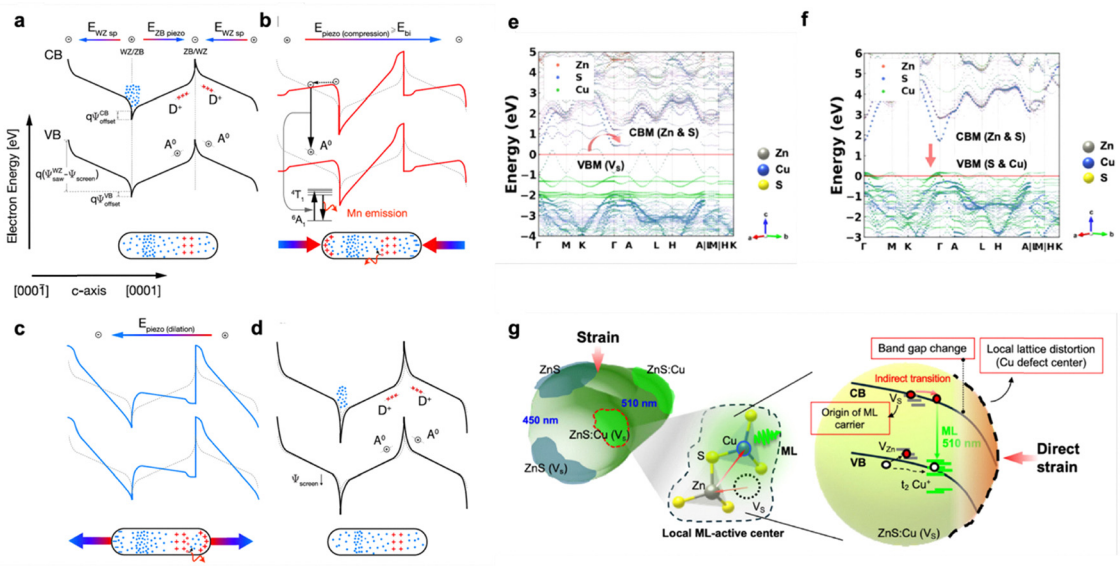

Fig. 5 (a) Schematic band diagram of faulted ZnS:Mn under no external stress, showing the WZ/ZB/WZ stacking sequence with charged interfaces formed by stacking faults. (b) Compressive strain enhances interfacial polarization and induces local band bending, promoting carrier accumulation at the fault boundaries. (c) Tensile strain further amplifies the internal field, facilitating carrier detrapping and radiative recombination at Mn^{2+} luminescent centers. (d) After multiple stress–release cycles, the lattice restores its original configuration, maintaining reversible and repeatable emission. Reproduced with permission from *ACS Nano* 2021, **15**, 4115. © American Chemical Society, (e) Density functional theory calculated band structure of Cu-doped ZnS with an S vacancy [ZnS:Cu(V_S)], showing strain-induced band-gap narrowing and mid-gap state formation. (f) Band structure of Cu-doped ZnS without an S vacancy [ZnS:Cu], confirming that Cu-related defect states reduce the local band gap. (g) Schematic summary of the defect-localized ML mechanism, where lattice distortion around Cu–S vacancy complexes modulates local fields and drives elastic ML emission near 510 nm. Reproduced with permission from *ACS Nano*, 2025, **19**, 35027. © American Chemical Society.

field. Identifying materials that satisfy one or both of these conditions is therefore essential for constructing polymer-based ML platforms capable of efficient, repeatable, and field-driven luminescence. This section establishes a consistent conceptual foundation for understanding how mechanical energy is converted into optical emission across different architectures and provides a rational basis for the next section, where polymer-induced triboelectric field coupling and its integration into ML platform are discussed in detail.

3. Polymer-based ML platforms

The integration of polymer matrices into ML solids marked a decisive turning point in overcoming the intrinsic limitations of solid-state phosphors. Conventional ML materials, though highly efficient in single-crystal or ceramic form, suffer from restricted strain tolerance, high stress thresholds, and rapid fatigue under repeated loading. These limitations hindered the realization of recoverable and scalable ML devices. The introduction of elastomeric polymers provided an elegant and practical solution, enabling mechanical flexibility, durability, and more importantly, an indirect yet highly effective route to generate internal triboelectric fields capable of driving luminescence.

3.1. The emergence of a polymer-based ML platform

The seminal work by Jeong *et al.* in 2013 reported the first polymer-integrated ML composite platform, establishing the foundation for subsequent flexible ML systems (Fig. 7a).[18] Embedding ZnS:Cu microparticles within a soft PDMS matrix enabled exceptionally bright, repeatable, and durable ML emission far beyond that of rigid ZnS:Cu phosphors (Fig. 7b). The composite (denoted as the ML platform in this study) maintained stable luminescence over 10^5 stretching–releasing cycles with minimal degradation and showed stress-rate-dependent color tunability from green to blue (Fig. 7c).

Although the mechanistic origin was not yet fully understood, the study revealed that the elastomeric PDMS matrix effectively transferred and redistributed mechanical stress to ZnS:Cu particles, preventing fracture and ensuring long-term operation. This pioneering finding demonstrated that incorporating a soft polymer not only improves mechanical compliance but also amplifies mechano-to-photon conversion, transforming ML into a flexible, stable, and tunable light-emission platform.

3.2. Color tunable and durable ML platforms by polymer integration

Following the 2013 breakthrough, subsequent works introduced color-controllable ML platforms using the same PDMS–ZnS:Cu system.[28] By combining ZnS:Cu,Mn and ZnS:Cu phosphors within a soft PDMS matrix, dual-band emission ranging from orange to green was achieved (Fig. 8a and b). Furthermore, by adjusting the mixing ratio between the two phosphors, the emission color could be finely tuned across the visible range (Fig. 8c and d).

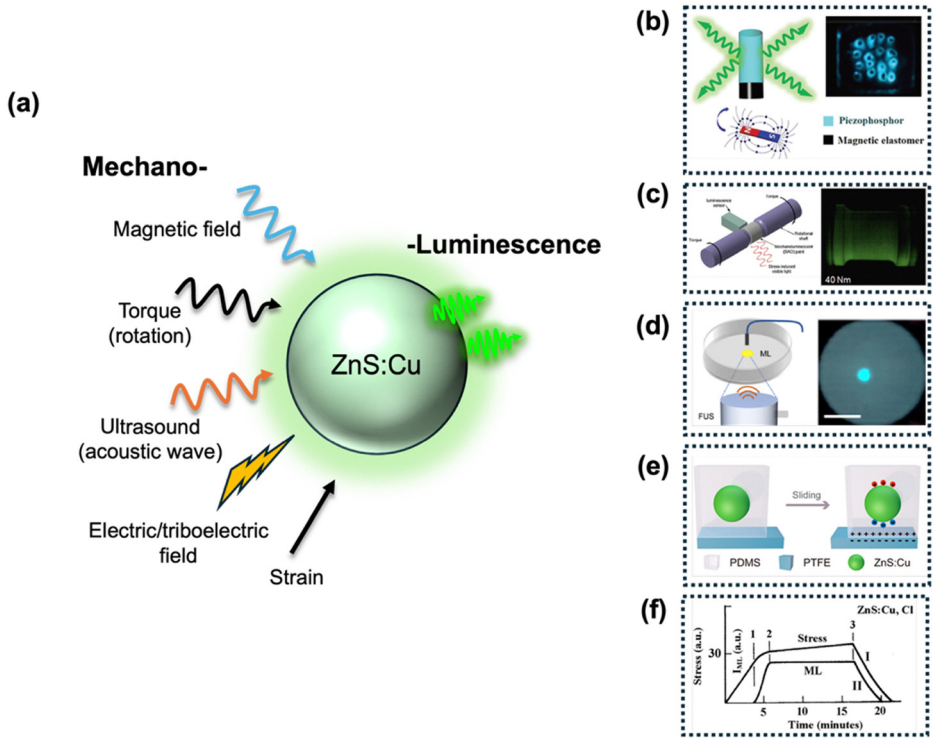

Fig. 6 (a) Schematic illustration of the ML properties of ZnS:Cu under various mechanical stimuli, including (b) magnetic field and (c) torque, (d) ultrasound, (e) triboelectric field, and (f) direct pressure. Reproduced with permission from *Adv. Mater.*, 2017, **29**, 1701945. Copyright © 2017 Wiley-VCH GmbH. Reproduced with permission from *Sens. Actuators A Phys.* 2014, **218**, 125–131. Copyright © 2014 Elsevier B.V. Reproduced with permission from *Nano Lett.* 2025, **25**, 11747–11755. Copyright © 2025 American Chemical Society. Reproduced with permission from *ACS Appl. Mater. Interfaces*, 2022, **14**, 4775–4782. Copyright © 2022 American Chemical Society. Reproduced with permission from *Physica B*, 2016, **491**, 12–16. Copyright © 2016 Elsevier B.V.

The integration of soft polymers allowed mechanical stimuli to be transferred uniformly to the phosphors, enabling continuous control of external stress and thereby color conversion through the superposition of multiple emission bands. These findings highlighted a key transition in ML research, showing that the polymer matrix evolved from a passive structural support into an active component that influences the overall luminescence behavior of the composite.

3.3. Influence of polymer properties on ML performance

Some studies revealed that the elasticity of the polymer matrix plays a decisive role in determining ML efficiency. In the pioneering work by Qian *et al.*,[45] the elastic modulus of PDMS was systematically tuned by incorporating different concentrations of SiO_x nanoparticles, which act as rigid fillers to enhance the matrix stiffness (Fig. 9a). As the SiO_x content increased, the elastic modulus rose nearly linearly, while the ML intensity exhibited a pronounced enhancement (Fig. 9b). This study suggested that stiffer matrices can more effectively transfer mechanical energy to the embedded ZnS phosphors, thereby amplifying the mechano-to-photon conversion process.

Similarly, a recent study in 2025 systematically investigated how the elasticity of PDMS influences ML performance by varying curing conditions to obtain low, medium, and high elasticity levels (Fig. 9c).[5] The relative ML intensity also decreased with increasing elasticity (Fig. 9d). These results indicate that achieving an optimal elastic modulus that ensures both sufficient deformability and efficient stress transfer is essential for maximizing ML efficiency in polymer–phosphor composites.

Furthermore, one of the important properties of the polymer was reported, demonstrating that the triboelectric field generated at the phosphor–polymer interface can serve as a decisive factor in governing ML performance.[46] In the LuAG:Ce^{3+}/PDMS system, the dynamic contact and separation between the dielectric surfaces of phosphor particles and polymer matrix induce charge transfer through contact electrification, forming a localized interfacial electric field (Fig. 9e). The triboelectric field strength, which varies among polymers such as PDMS, polyurethan (PU), and silicone rubber (SC) due to their different dielectric constants and surface energies, directly affects ML intensity (Fig. 9f), confirming that interfacial electrification plays a critical role in determining overall luminescence efficiency.

The causal role of the triboelectric field in driving ML was further verified through a direct electroluminescence experiment, where the intrinsic triboelectric potential of each polymer was applied to a ZnS:Cu layer.[5] In this setup (Fig. 9g), a pure polymer film was connected to a ZnS:Cu single layer *via* an aluminum electrode, allowing the contact-electrification-induced voltage to act as an external driving field. The surface charge density and output voltage exhibited a clear polymer-

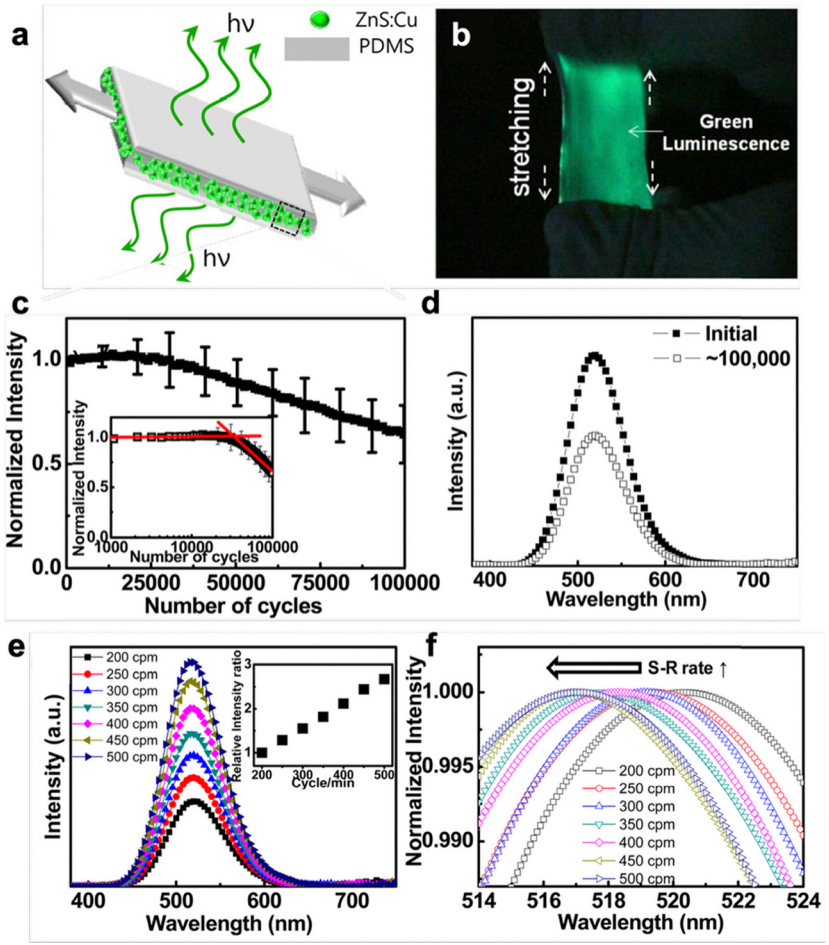

Fig. 7 (a) Schematic illustration and (b) photograph of the polymer-intergrated ML platform under tensile deformation, demonstrating bright and uniform ML emission. (c) Average normalized ML intensity as a function of stretching–releasing (S–R) cycles, showing stable luminescence even after 10^5 cycles. (d) Comparison of ML intensity between the initial and 10^5 cycle states. (e) Evolution of ML spectra and (f) normalized emission profiles with increasing S–R rate, revealing stress-rate-dependent color tunability from green to blue. Reproduced with permission from *Appl. Phys. Lett.*, 2013, **102**, 051110. © 2013 American Institute of Physics.

dependent trend (Fig. 9h), following epoxy resin (ER) < PU < PDMS < eco-flex (EF) < dragon-skin (DS). When the same potential was applied to the ZnS:Cu layer, the resulting AC-electroluminescence spectra (Fig. 9i) showed linearly increasing brightness consistent with the triboelectric polarity sequence. This direct correspondence provided unambiguous experimental evidence that the interfacial triboelectric field of the polymer matrix governs the emission behavior of ZnS phosphors, thereby reaffirming the previously discussed triboelectric-driven ML mechanism.

3.4. Diversification of core–polymer composites for advanced ML platforms

Building on the foundational PDMS–ZnS:Cu system, subsequent research has rapidly expanded both the phosphor core compositions and polymer matrix types, giving rise to a diverse family of polymer-integrated ML films.[18] This diversification was driven by two major goals: (i) to tailor the spectral and mechanical characteristics of emission and (ii) to optimize interfacial triboelectric coupling for higher efficiency and functionality.

Early demonstrations extended the polymer integration concept beyond ZnS-based phosphors to systems such as $SrAl_2O_4$:Eu^{2+},Dy^{3+} and CaZnOS:Tb^{3+},[47] where embedding within elastomeric matrices such as PDMS, PU, and SC enabled stretchable, recoverable, and strain-dependent luminescence. Subsequent studies further diversified the polymer types to include materials with distinct dielectric constants and triboelectric polarities, such as polyvinylidene fluoride (PVDF), Ecoflex, and Dragon Skin, to modulate interfacial electric fields and emission intensity. At the same time, integration with rigid or oxide-based ML phosphors (*e.g.*, $Sr_3Al_2O_6$:Eu^{2+} and $BaSi_2O_2N_2$:Eu^{2+})[48] through PDMS or epoxy hybrid matrices demonstrated improved piezophotonic coupling and mechanical durability.

Despite the increasing diversification of polymer-integrated ML films, most reported systems have relied on empirically chosen polymers rather than mechanism-guided design. This underscores the need for clearer selection principles, which we discuss in detail in Section 4.5 (Table 1).

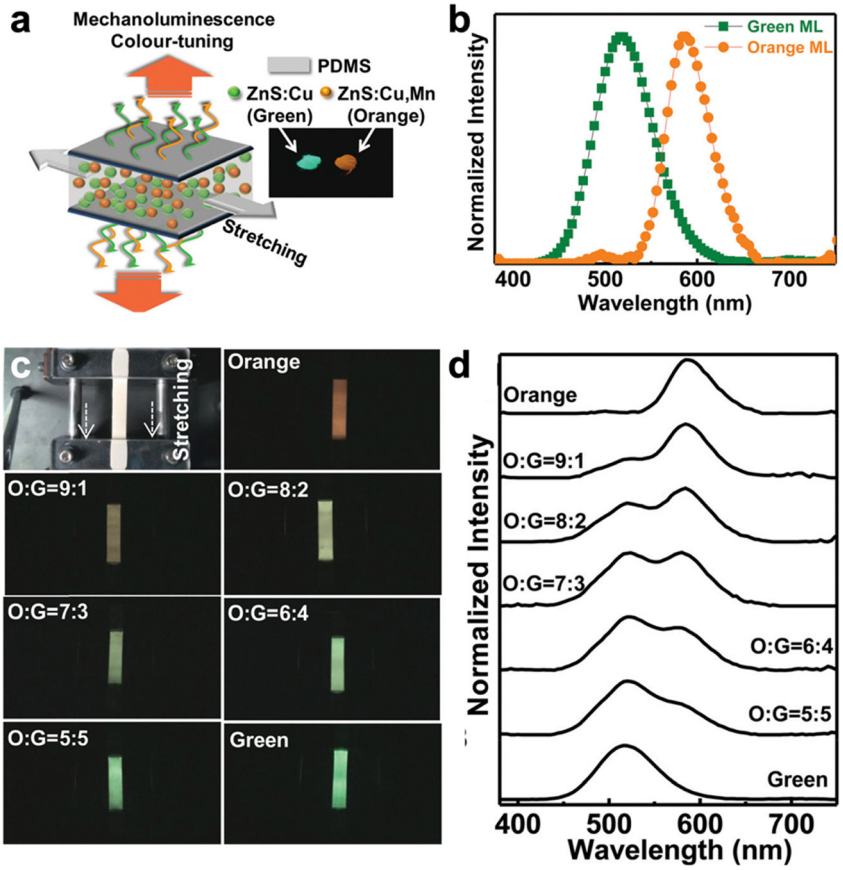

Fig. 8 (a) Schematic illustration and (b) representative spectra of ZnS:Cu,Mn (orange) and ZnS:Cu (green) phosphor embedded in a PDMS matrix (ML platform), showing dual-color emission characteristics. (c) Photographs of ML platforms with different orange-to-green (O : G) ratios under cyclic stretching and (d) corresponding ML spectra at various O : G ratios, demonstrating continuous color tuning from orange to green through polymer-assisted control of mechanical excitation. Reproduced with permission from *Adv. Mater.*, 2013, **25**, 6194. © 2013 WILEY-VCH Verlag GmbH & Co. KGaA.

3.5. Conceptual summary

From the previous polymer-based ML studies, the evolution of polymer-integrated ML materials represents a continuous transformation in perspective. Initially, polymers were regarded merely as structural supports, providing durability and strain compliance to protect the embedded phosphors. Over time, however, they came to be recognized as active charge-field mediators, capable of converting mechanical stimuli into interfacial triboelectric fields that drive luminescence. This transition fundamentally redefined the ML paradigm, from purely mechanically induced emission to electrically mediated elastic luminescence. These discoveries laid the foundation for subsequent advances in triboelectric-field-assisted ML platforms, where the triboelectricity and elasticity of the polymer matrix emerged as key determinants of light output efficiency.

4. Working principles of polymer-based ML platforms

As discussed in the previous section, integrating elastomeric polymers into ML systems enabled not only mechanical flexibility and durability but also an entirely new mechanism of light generation. In contrast to rigid solid-state ML, where direct lattice deformation induces piezopotentials, polymer-based ML platforms operate through interfacial triboelectric coupling, in which mechanical energy is first converted into an electric field at the polymer–phosphor interface. This section summarizes the working principles of such polymer-mediated ML systems, focusing on how triboelectric interactions, elasticity, and piezophotonic effects collectively govern their performance.

4.1. Interfacial triboelectric field formation in polymer–phosphor composites

The 2019 study conducted by Park *et al.* provided one of the earliest direct visualization of how interfacial triboelectric fields arise in polymer–phosphor composites.[19] Using a woven ZnS:Cu–PDMS/PTFE (polytetrafluoroethylene) textile architecture, they demonstrated that mechanical motion induces dual electric field formation (internal and external triboelectrification) responsible for light generation under both compression and separation.

In ML textile architecture, the elastic deformation of the PDMS matrix induces microscopic pore generation at the polymer–phosphor boundary (Fig. 10a). During compression and release, these pores alternately form and collapse, allowing

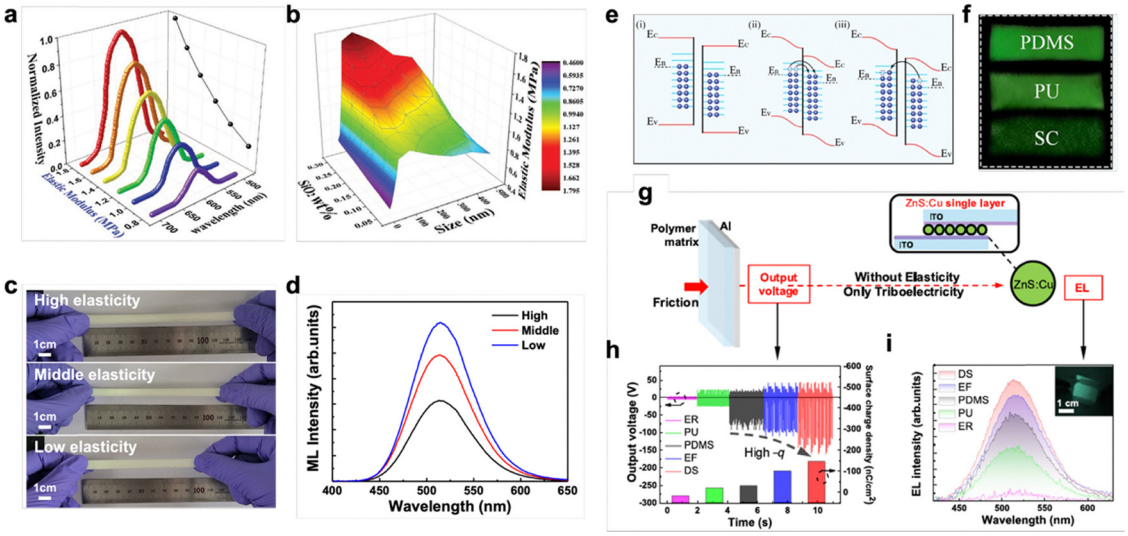

Fig. 9 (a) Variation of the elastic modulus of PDMS as a function of SiO_x nanoparticle concentration, showing a monotonic increase in stiffness with filler loading. (b) Corresponding ML intensity of the SiO_x-doped ML platform under identical strain conditions, demonstrating that higher matrix stiffness leads to stronger ML emission. (c) Photograph of strain testing for PDMS-based ML platforms with different elasticities. (d) Relative ML intensity as a function of polymer elasticity, showing that increased elasticity results in reduced ML brightness. (e) Schematic illustration of the contact-electrification-induced charge-transfer process at the phosphor–polymer interface, showing the formation of a localized electric field during dynamic contact and separation. (f) Photographs and ML intensities of LuAG:Ce^{3+} phosphors embedded in different polymers (PDMS, PU, and SC), demonstrating that the triboelectric polarity and dielectric properties of the matrix govern the overall ML brightness. (g) Schematic diagram of the experimental setup used to apply the contact-electrification-induced voltage of a pure polymer film to a ZnS:Cu single layer, isolating the effect of triboelectric potential. (h) Output voltage and surface charge density of different polymer matrices (ER, PU, PDMS, EF, and DS), showing a systematic increase in negative triboelectricity. (i) AC-electroluminescence spectra of ZnS:Cu driven by the triboelectric field of each polymer, confirming that ML brightness follows the same polymer-dependent trend. (a) and (b) are reproduced with permission from *Adv. Mater.*, 2018, 30, 1800291. © 2018 Wiley-VCH Verlag GmbH & Co. KGaA. (e) and (f) are reproduced with permission from *Nano Energy*, 2022, **94**, 106920. © 2022 Elsevier Ltd. (c), (d), (g), (h) and (i) are reproduced with permission from *Nat. Commun.*, 2025, **16**, 854. © The Authors, CC BY 4.0.

Table 1 Representative polymer–phosphor composite systems for flexible and efficient ML platforms

Phosphor core	Polymer matrix	Key characteristics/functionality	Ref.
ZnS:Cu/ZnS:Mn	PDMS	Foundational ML composite; bright, repeatable emission for wearable sensing	26
$SrAl_2O_4:Eu^{2+},Dy^{3+}$	Silicone rubber/PU/PDMS	Flexible, strain-dependent luminescence; used in stress mapping and displays	18
CaZnOS:Tb^{3+}/Mn^{2+}	PDMS/Ecoflex	Piezoelectric coupling in a wurtzite lattice; e-signature and tactile sensing	18
CaZnOS:Sm^{3+}	PDMS	Stable red ML; elasticity-tuned emission for multicolor displays	41
ZnS:Cu,Mn	PU/PVDF/PDMS	Polymer-dependent triboelectric field controls ML brightness and recoverability	40
$Sr_3Al_2O_6:Eu^{2+}$	PDMS/epoxy resin	Hybrid structure combining rigidity and elasticity for improved piezophotonic coupling	22
$BaSi_2O_2N_2:Eu^{2+}$	PU/PDMS hybrid	Transparent ML composite film for optical and motion sensing	42

triboelectric charge accumulation and separation between the negatively charged PDMS and the positively charged ZnS:Cu surface. This dynamic pore behavior produces localized interfacial potentials acting as nanoscale capacitors, where the internal electric field strength is directly modulated by the degree of interfacial separation.

This mechanism is further supported by Fig. 10b, which illustrates the presence of both internal (ZnS–PDMS) and external (PDMS–Kapton or PTFE) triboelectric interfaces. Mechanical deformation activates charge transfer across these boundaries, forming alternating local fields that act cooperatively to trigger light emission. In this combined field environment, trapped carriers within ZnS:Cu are released and recombine radiatively at Cu^+ luminescent centers, as schematically depicted in Fig. 10c. Moreover, Fig. 10d and e quantitatively demonstrate that the strength of the triboelectric field is a decisive factor governing ML brightness. Increasing the surface charge density or contact potential difference directly enhances emission intensity, confirming that luminescence efficiency scales with the interfacial field magnitude rather than with applied mechanical stress.

Collectively, these results established the fundamental interfacial triboelectric excitation model, where light emission originates from dynamically generated electric fields at elastic polymer–phosphor interfaces, not from direct lattice distortion. This study laid the conceptual groundwork for understanding triboelectric-field-driven ML in later polymer-integrated systems.

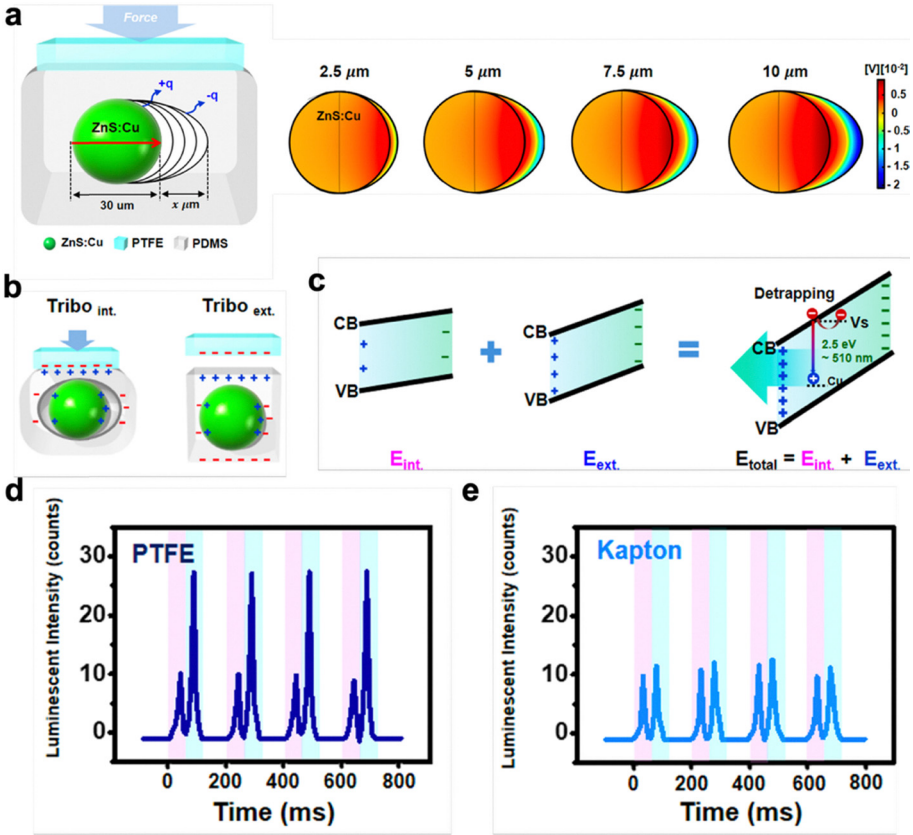

Fig. 10 (a) Microscopic pore formation and charge separation at the ZnS:Cu–PDMS interface during elastic deformation. (b) Schematic illustration of dual triboelectric interfaces (internal ZnS–PDMS and external PDMS–PTFE) governing local electric field generation. (c) Band diagram showing carrier detrapping and radiative recombination under triboelectric field–induced band bending. (d) and (e) Correlation between the triboelectric potential difference and mechanoluminescence (ML) brightness for devices using polytetrafluoroethylene (PTFE) and Kapton interfaces, respectively, confirming the electric field magnitude as a dominant factor in emission efficiency. Reproduced with permission from *ACS Appl. Mater. Interfaces*, 2019, **11**, 5200. © 2019 American Chemical Society.

4.2. Simulation-based verification of the interfacial triboelectric field

Based on the interfacial triboelectric excitation mechanism, Lee *et al.* further investigated how the triboelectric field formed at the polymer–phosphor interface contributes to ML through finite-element electric-field simulations.[22] The study modeled an AlO_x-coated ZnS:Cu microparticle embedded in a PDMS matrix, assuming realistic interfacial charge densities derived from triboelectric measurements ($\approx$35 μC m^{-2}) and geometric parameters corresponding to experimental composites.

As shown in Fig. 11a and b, the simulated electric-field distribution under a uniform external field (10^6 V m^{-1}) revealed that the internal field within ZnS:Cu is roughly half of the applied field, defining the "turn-on" field ($E_{on} \approx 0.5 \times 10^6$ V m^{-1}) required for electroluminescence activation. In Fig. 11c and d, introducing a microscopic interfacial gap with uniformly distributed triboelectric charges (±35 μC m^{-2}) increased the internal field only up to 0.2×10^6 V m^{-1} (insufficient to trigger emission). However, when localized charge accumulation was considered representing non-uniform triboelectric charge distribution over ≈40% of the interface (Fig. 11e and f), the resulting field intensity exceeded the E_{on} threshold ($\approx 1.6 \times 10^6$ V m^{-1}).

This localized triboelectric field was strong enough to activate more than 70% of the ZnS:Cu particle volume, providing direct theoretical support for triboelectric-field-driven carrier excitation rather than purely mechanical activation. These simulation results quantitatively validate that microscale charge concentration and interfacial geometry critically govern the triboelectric potential in ZnS:Cu–PDMS systems, confirming that the experimentally observed ML originates from an internal interfacial triboelectric field strong enough to induce electroluminescence.

4.3. Experimental and theoretical evidence of the interfacial triboelectric-induced ML

A comprehensive mechanistic framework for polymer-based ML platforms has been established by combining structural, mechanical, and theoretical insights from recent studies. As illustrated in Fig. 12a, the ML platform consists of solid-state phosphors such as ZnS:Cu microparticles uniformly embedded in an elastic polymer matrix, where interfacial contact and separation generate triboelectric potentials upon

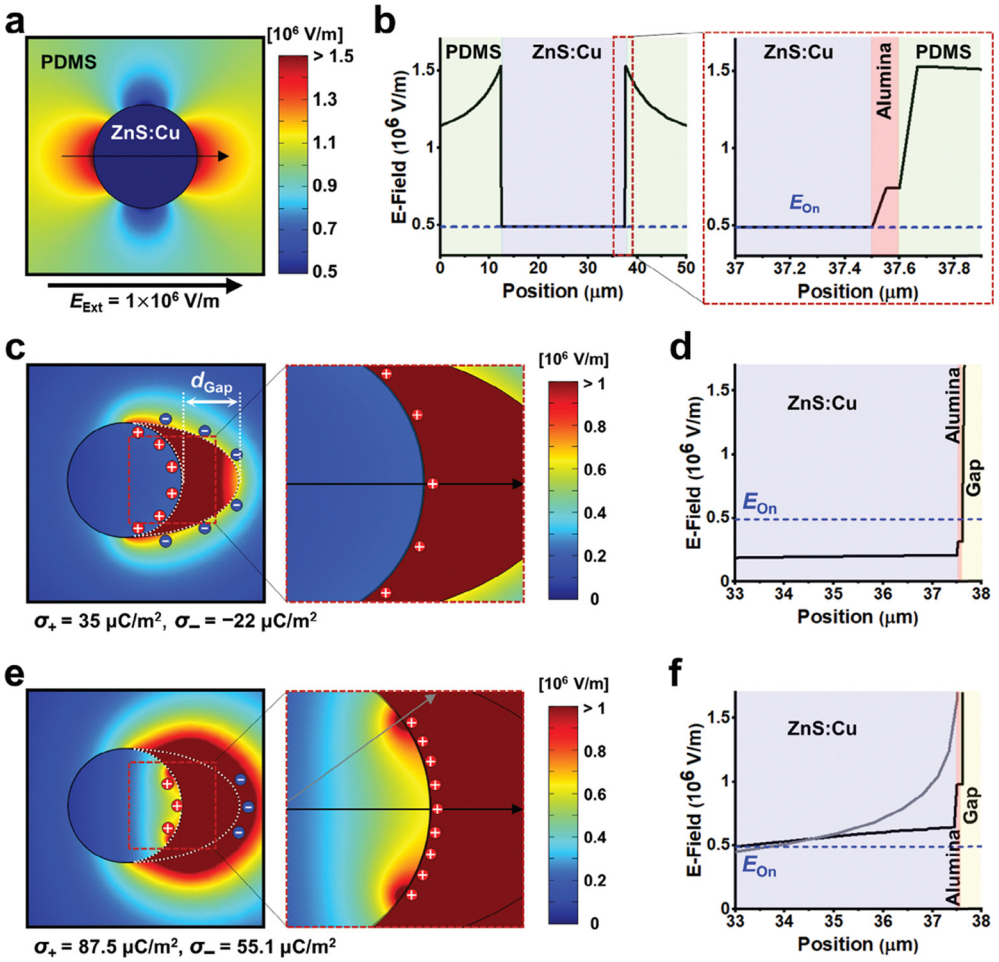

Fig. 11 (a) Simulated electric-field distribution in ZnS:Cu–PDMS composites under a uniform external field ($E_{on} \approx 0.5 \times 10^6$ V m^{-1}). (b) Cross-sectional field profile across a ZnS:Cu particle showing a constant internal field at the turn-on level. (c) Electric-field distribution with a uniform interfacial gap containing oppositely charged triboelectric layers. (d) Weak internal field near the charged surface, below the emission threshold. (e) Electric-field distribution with localized triboelectric charge accumulation over 40% of the interface. (f) Amplified internal field exceeding E_{on}, confirming that localized interfacial charges can activate ML emission. Reproduced with permission from *Small*, 2024, **20**(17), 2307089. © 2024 Wiley-VCH GmbH.

mechanical deformation. The soft, negative-triboelectric polymer not only accommodates reversible strain but also forms dynamic interfacial pores that act as charge storage and emission sites during cyclic stress.

Recent reports have provided converging experimental and theoretical evidence for this pore-mediated excitation mechanism. Finite-element simulations directly confirmed the formation of a microscopic interfacial pore gap under strain and its role in generating localized triboelectric fields (Fig. 12b–h).[5] The simulated electric-field maps revealed that asymmetric pore structures amplify local field strength beyond 3×10^6 V m^{-1}, while excessive pore expansion weakens charge concentration (Fig. 12b–d). Scanning electron microscopy visualized nanoscale pores at the ZnS:Cu–PDMS boundary (Fig. 12e and g), while optical ML mapping (Fig. 12f and h) confirmed that samples with dense, uniformly distributed pores exhibit higher and more homogeneous emission than those with enlarged or irregular gaps. Collectively, this study suggested that the degree of interfacial porosity directly modulates triboelectric field strength and thus governs overall ML efficiency.

Complementary studies on non-piezoelectric systems further support this mechanism. In CaF_2:Tb^{3+}/PDMS elastomers, ML occurs exclusively at the moment of interfacial detachment rather than during continuous strain (Fig. 12i), indicating that transient charge recombination, rather than lattice deformation, is responsible for light generation.[49] Dye-infiltration imaging (Fig. 12j) visualized the nanoscale gaps that form during stretching, directly revealing charge-accumulating voids at the polymer–phosphor interface. The charge-transfer process is schematically summarized in Fig. 12k and l, where electrons move from the PDMS surface to the more electronegative phosphor upon stretching, followed by rapid recombination during relaxation that excites luminescent centers such as Cu^+ or Tb^{3+}. This reversible charge–discharge behavior explains the bright and recoverable emission of polymer-based ML composites.

Taken together, Fig. 12 establishes a unified mechanistic view that ML in polymer–phosphor composites arises from

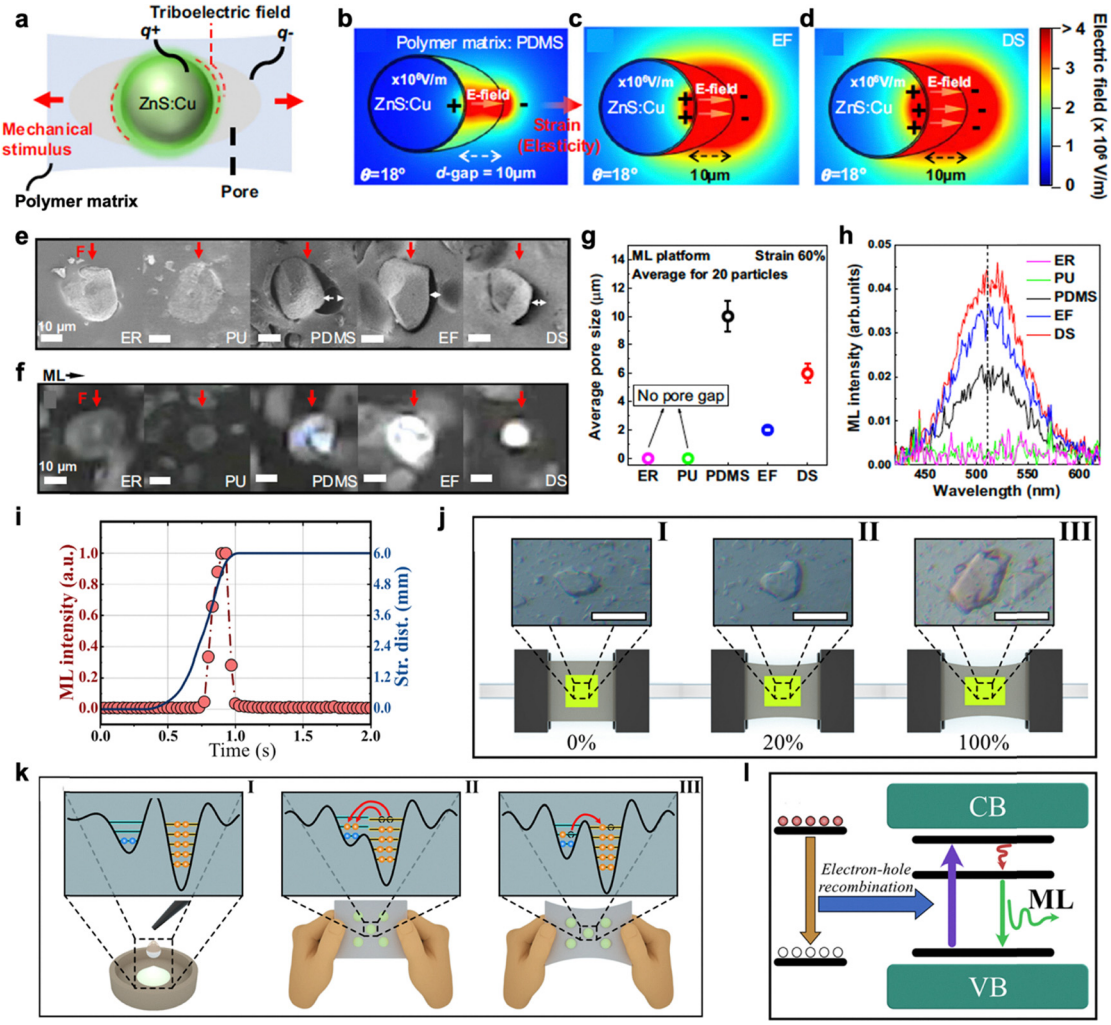

Fig. 12 Working mechanism and interfacial field characteristics of the polymer-integrated mechanoluminescent (ML) platform. (a) Schematic illustration of the ML process in an elastic polymer matrix containing ZnS:Cu phosphors. (b)–(d) Finite-difference time-domain (FDTD) simulations of the triboelectric field across the interfacial gap (10 μm) between ZnS:Cu and different polymer matrices: (b) PDMS, (c) Ecoflex (EF), and (d) dragon skin (DS), showing distinct charge density distributions. (e) and (g) SEM images and corresponding average interfacial gap (dgap) values between ZnS:Cu and each polymer under 60% strain (error bars represent 11% deviation). (f) and (h) ML emission images and spectra of single ZnS:Cu particles depending on the polymer type under 60% strain. (i) Variation of ML intensity with the stretching distance during a single elongation cycle. (j) Optical microscopy images of the elastomer before stretching (I) and after 20% (II) and 100% (III) deformation. (k) Schematic representation of electron potential well evolution and charge transfer in phosphor–polymer interfaces under strain, illustrating triboelectric-field–assisted excitation of Tb^{3+} emitters *via* electron–hole recombination and energy transfer. Reproduced with permission from *Nat. Commun.*, 2025, **16**, 854. © The Authors, CC BY 4.0. Reproduced with permission from *Nat. Commun.*, 2022, **13**, 6542. © The Authors, CC BY 4.0.

dynamically modulated interfacial triboelectric fields, where the cyclic formation and annihilation of nanoscale pores regulate charge accumulation and radiative recombination. The polymer matrix acts as a mechanical buffer and charge mediator, enabling bright, stable, and self-recoverable emission that characterizes next-generation polymer-based ML platforms.

4.4. Unified mechanistic model of polymer-based ML systems

The operation of polymer-based ML platforms can be understood as a cyclic electromechanical process governed by interfacial field coupling rather than direct lattice deformation. When mechanical strain is applied, periodic contact and separation at the polymer–phosphor interface generate triboelectric charges that form localized electric fields (E_t). These interfacial fields polarize the phosphor lattice, inducing an additional piezoelectric component (E_p), and the combined potential ($E_t + E_p$) modulates trap levels to facilitate carrier detrapping and radiative recombination. Upon stress release, the elastic polymer restores its original configuration and reestablishes interfacial contact, allowing continuous charge–discharge cycling and self-recoverable emission. This interfacial triboelectric field–driven piezo-photonic mechanism unifies the previously separate interpretations of ML based on piezoelectric, triboelectric, and contact-electrification effects. It explains why polymer-based systems exhibit high brightness,

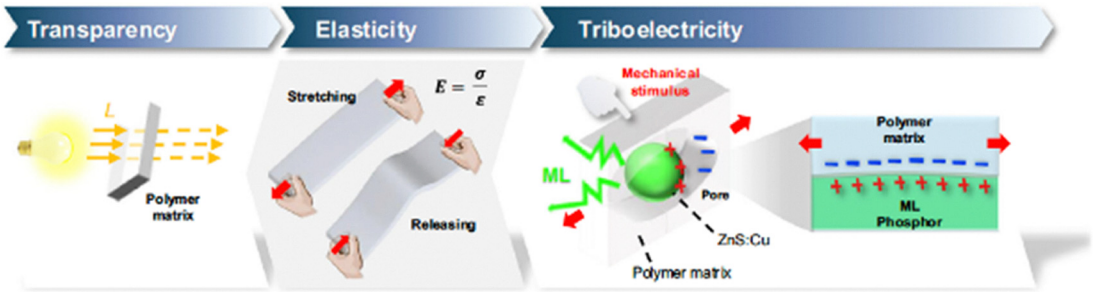

Fig. 13 Schematic illustration of the polymer matrix selection strategy guided by three principal parameters: optical transparency, mechanical elasticity, and triboelectric polarity. Reproduced with permission from *Nature Communications*, 2025. © 2025 Springer Nature. All rights reserved.

low activation stress, and superior durability compared to rigid counterparts, providing the physical foundation for the design principles discussed in the following section.

4.5. Design strategies for high-performance ML platforms with elastic polymers

The evolution of polymer-based ML platforms reveals a paradigm shift from stress-driven to field-driven luminescence. The emission efficiency and stability are governed not by the magnitude of mechanical deformation but by the quality of interfacial field coupling, which is dictated by the elasticity, dielectric behavior, and triboelectric polarity of the polymer matrix. Building on these principles, high-performance polymers must satisfy several key criteria (Fig. 13).

First, optical transparency is essential because ML emission generated within the phosphor must pass through the polymer without scattering or absorption loss. Any reduction in transparency directly decreases the external photon output, making polymer optical clarity a fundamental requirement for preserving the intrinsic emission efficiency.

Second, mechanical elasticity plays a central role in facilitating triboelectric field formation at the phosphor–polymer interface. Under mechanical deformation, elastic polymers allow controlled formation of interfacial micro-gaps, which act as sites for charge separation. However, if the elasticity is too high and the gaps become excessively small, the generated triboelectric field can diminish, leading to reduced ML efficiency. Therefore, elasticity must be considered in conjunction with additional factors that preserve adequate interfacial spacing for effective field generation.

Third, given this interfacial mechanism, strong negative triboelectric polarity becomes a decisive criterion. Even when the interfacial gaps are small, polymers with highly negative triboelectric characteristics can accumulate substantial charge density, thereby maximizing the local electric field and sustaining high ML output. For this reason, achieving simultaneous enhancement of elasticity and efficiency requires a balanced consideration of both elastic properties and triboelectric polarity.

Taken together, these considerations highlight that polymer selection cannot be arbitrary or empirical. Instead, it should be guided by the intrinsic ML mechanism of the phosphor and by the field-coupling characteristics of the polymer matrix. The framework presented here provides a mechanistic basis for rational polymer design and offers practical guidance for developing next-generation ML platforms with enhanced efficiency, stability, and mechanical resilience.

5. Emerging and broad-spectrum applications of ML platforms

With the advent of polymer-based ML platforms, the field of ML has entered a stage of rapid expansion. The elastic polymer matrix not only enables the activation of intrinsic solid-state phosphors with repeatable and high ML performance under very weak mechanical stimuli but also provides morphological freedom required for diverse application environments. The unique combination of high flexibility, strong emission performance, and self-recoverable characteristics has propelled polymer-based ML platforms from fundamental research to diverse real-world applications. This section widely provides an overview of the applications of ML platforms in stress sensing, motion monitoring for healthcare, and biomedical technologies.

5.1. Stress-sensing

With the integration of polymer matrices into solid-state ML phosphors, their capability for stress sensing has been greatly enhanced, enabling highly sensitive and self-powered visualization of mechanical stimuli without external energy input. In particular, their morphological freedom allows the design of pressure sensors adaptable to diverse application environments.

One of the earliest demonstrations of this concept in soft robotics was presented by Zhuang and Xie, who highlighted the potential of the ZnS:Cu–PDMS ML platform for real-time stress visualization in flexible robotic systems.[50] When integrated onto robotic joints or actuators, these ML–polymer hybrids emitted light in response to localized strain, allowing distributed mapping of stress propagation and contact pressure during dynamic motion (Fig. 14a). The elastomeric polymer matrix provided conformal contact to curved robotic surfaces, ensuring reproducible optical response under repeated deformation. Such self-reporting luminescent layers established a

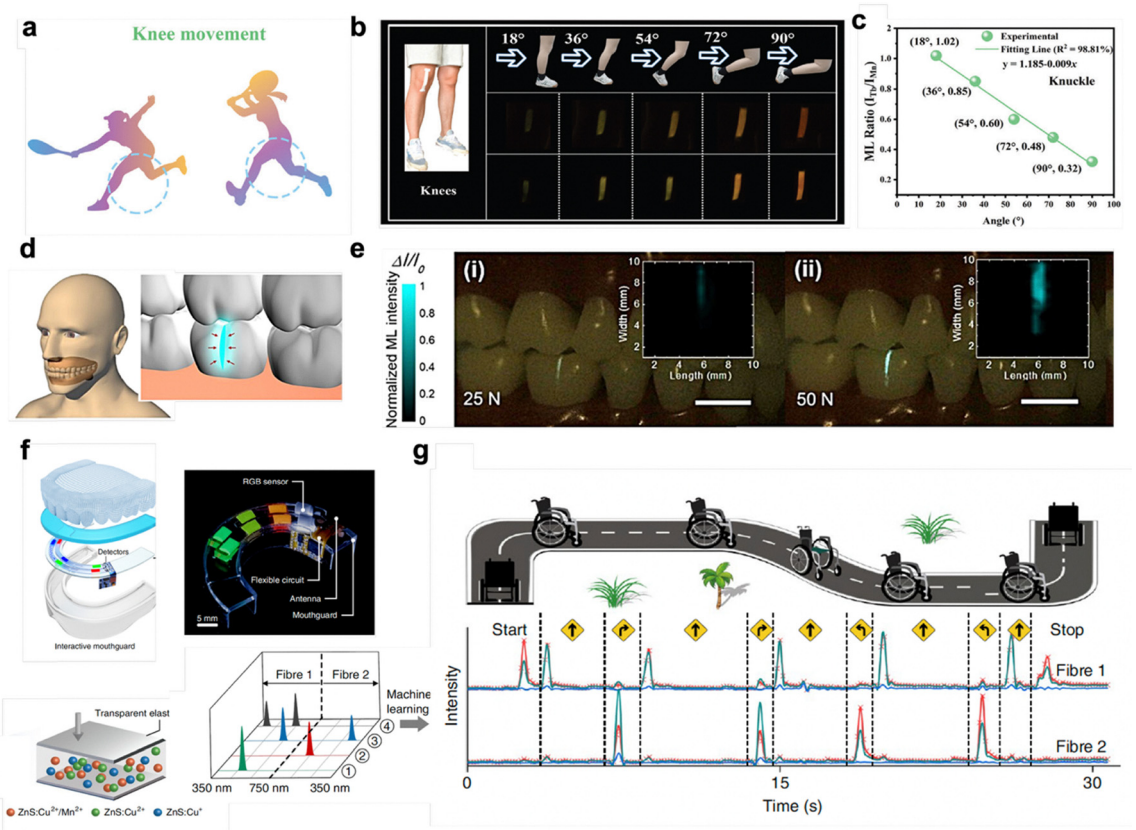

Fig. 14 (a) Schematic illustration of different human joint movements monitored by ML sensors. (b) Photographs of the CAP:Tb^{3+}, Mn^{2+}@PDMS composite attached to a knee joint, showing angle-dependent ML emission during bending. (c) Variation in the integrated emission-intensity ratio (I_{Tb}/I_{Mn}) of the same composite on a finger joint under different bending angles, demonstrating ratiometric strain sensing. (d) Schematic illustration of light generation from ZRT phosphor particles embedded in cracked regions. (e) Photographs of a denture specimen containing micro-cracks filled with ZRT phosphors, visualizing stress-induced luminescence. (f) Design of the ML-powered distributed-optical-fiber (mp-DOF) sensor integrated into an elastomeric mouthguard. The inset shows the multilayer architecture of the device comprising the mouthguard, multicolor ML contact array, and flexible circuit module. (g) Demonstration of wheelchair navigation controlled by bite-induced luminescent signals from the mouthguard sensor, with the corresponding real-time optical output and motion trajectory displayed. Reproduced with permission from T. Wang *et al.*, *Advanced Science* 2025, **12**, 2410673. © 2024 The Author(s). Panels (a)–(c) are published by Wiley-VCH GmbH under the Creative Commons Attribution License (CC BY 4.0). Panels (d) and (e) are reproduced with permission from *NPG Asia Materials* 2022, **14**, 26. © The Author(s) 2022. Published under the Creative Commons Attribution 4.0 International License (CC BY 4.0). Panels (f) and (g) are reproduced with permission from *Nature Electronics* 2022, **5**, 693–702. © The Author(s) 2022. Published under a Creative Commons Attribution 4.0 International License (CC BY 4.0).

new paradigm for adaptive and intelligent robotics capable of autonomous monitoring through visual feedback (Fig. 14b and c). Even in the submicron gaps of irregular dental cracks where conventional stress sensors cannot be applied effectively, the elastic polymer matrix exhibited remarkable morphological adaptability, conformally embedding the ML phosphors and enabling precise detection of occlusal forces through luminescent feedback.[51] In this unique system, ML emission from submicron cracks was transduced into photocurrent signals under masticatory forces, enabling two-dimensional mapping of stress concentration and early-stage tooth fractures (Fig. 14d and e). This work demonstrated that ML can serve not only as a structural stress indicator but also as a diagnostic tool for noninvasive health monitoring.

More recently, Hou *et al.* reported a ML mouthguard sensor that fully exploited the morphological flexibility provided by an integrated elastomeric polymer matrix.[52] The polymer-based design enabled the fabrication of a conformable mouthguard-shaped ML platform capable of adhering seamlessly to curved dental surfaces (Fig. 14f). Owing to this flexibility and mechanical compliance, the device exhibited exceptionally high sensitivity, producing distinguishable luminescence responses corresponding to various biting intensities and patterns during mastication (Fig. 14f). By leveraging the high sensitivity of the ML platform during bite motion, the system was able to generate multiple distinguishable luminescence signals corresponding to different occlusal patterns, ultimately enabling precise control of assistive devices such as wheelchairs and demonstrating its remarkable application potential (Fig. 14g). Due to this remarkable potential, recent research has increasingly focused on maximizing the resolution and multiplicity of signals in ML platforms for practical use.[53] These studies collectively demonstrate how the integration of polymer matrices into ML solids has profoundly expanded their

functional scope, clearly revealing the transformative impact of polymer engineering in enabling advanced, versatile, and application-oriented mechanoluminescent platforms.

5.2. Healthcare motion monitoring sensors

Owing to their high elasticity, strong luminescence response to subtle mechanical motions, and excellent durability under repeated stretching, polymer-based ML platforms have enabled the development of fiber-based optical sensors capable of detecting and visualizing human motion in real time.

As one of the earliest motion-driven sensors in the ML field, Qian *et al.* developed skin-driven ML platforms, in which ZnS:Mn phosphors were embedded in a PDMS-based elastomeric matrix doped with SiO_2 nanoparticles to tune its mechanical stiffness.[45] By increasing the matrix modulus, the polymers achieved stronger stress transfer to the embedded ZnS:Mn phosphors and consequently higher ML brightness, while maintaining flexibility for conformal skin attachment (Fig. 15a). Although this approach demonstrated the ability to capture minute facial muscle motions, including expression variations, the overall detectable deformation range was constrained by the intrinsic elasticity limit of PDMS (Fig. 15b).

In parallel, Zhou *et al.* reported a ML-triboelectric bimodal sensor (MTBS) that fully exploited the triboelectric potential provided by PDMS polymer surfaces.[54] As shown in Fig. 15c, the microstructured PDMS surface significantly enhanced charge density and enabled high triboelectric output, resulting in a self-powered, multimodal sensing platform for human-motion recognition. Although this design successfully achieved signal visualization and stable electrical readout for operating electronic devices, its performance remained confined to a narrow deformation range due to the intrinsic softness of PDMS, which limited effective stress transfer and thus restricted large-scale motion sensing. These results collectively emphasize that optimizing and diversifying polymer matrices beyond PDMS is essential to expand the mechanical adaptability and sensing resolution of ML-based motion sensors for human movement detection.

In contrast to previous studies that focused separately on elasticity or triboelectricity, a recent work placed the polymer matrix itself at the center of ML design.[5] As shown in Fig. 15d, a highly elastic and negatively triboelectric polymer matrix composed of polybutylene adipate-*co*-terephthalate (Ecoflex) and polycarbonate (Dragon Skin) was developed to simultaneously enhance interfacial field strength and mechanical compliance. This dual-functional matrix effectively coupled elastic deformation with triboelectric charge generation, resulting in intense and stable ML even under strains exceeding 100% (Fig. 15e). The fabric-type ML sensors achieved a luminance of approximately 139 cd m^{-2} and produced clear, motion-correlated optical signals during human joint movement without external power input (Fig. 15f). Unlike conventional PDMS-based systems, this study emphasized the decisive role of polymer characteristics such as modulus, triboelectric polarity, and dielectric constant in determining both ML intensity and deformation range. These results highlight that further development of diverse polymer matrices with tailored mechanical and electrical properties will be essential for expanding the

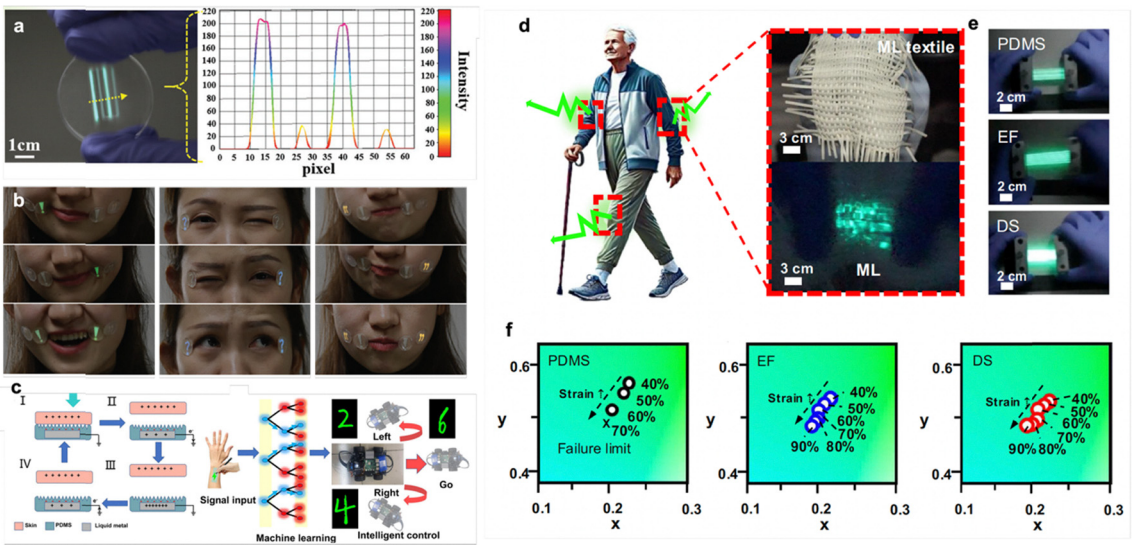

Fig. 15 (a) Comparison of ML intensity for different polymer matrices. The inset shows the intensity profile along the indicated arrow. (b) Skin-driven multicolor ML responses corresponding to facial muscle movements, including the lip corner, canthus, and cheek. (c) An intelligent control system for recognizing handwritten digits based on an interdisciplinary machine learning approach. (d) Schematic illustration of human motion detection (arm and knee bending) using the ML textile platform. The inset shows a photograph of the ML textile sensor composed of Dragon Skin (DS) and the corresponding emission image under weak stretching. (e) ML emission images of five fiber strands fabricated with PDMS, Ecoflex (EF), and DS matrices. (f) CIE color coordinates of ML textile sensors with PDMS, EF, and DS matrices, recorded during knee bending at strains exceeding 40%. Reproduced with permission from *Advanced Materials*, 2018, **30**, 1800291. © 2018 Wiley-VCH Verlag GmbH & Co. KGaA, Weinheim. Reproduced with permission from *Nano-Micro Letters*, 2023, **15**, 72. © The Author(s) 2023. Published by Springer Nature. Licensed under a Creative Commons Attribution 4.0 International License (CC BY 4.0). Reproduced with permission from *Nature Communications*, 2025. © 2025 Springer Nature. All rights reserved.

operational range and sensitivity of future ML-based motion-sensing platforms.

5.3. Biomedical technologies

ML platforms have recently been successfully extended into biomedical engineering, owing to the integration of elastomeric polymer matrices that endow them with flexibility, biocompatibility, and morphological adaptability essential for interfacing with soft biological tissues and artificial sensory systems.[55]

As summarized in Fig. 16a and b, polymer-based ML platforms have been successfully utilized to realize artificial cochlear and ocular devices.[56] In this system, an ML basilar membrane composed of an elastomeric matrix embedded with phosphors translated acoustic vibrations into spatially resolved optical signals, demonstrating frequency-selective light emission analogous to the tonotopic response of the human cochlea (Fig. 16c and d).

Such flexible ML platforms have also been applied to the eye for intraocular pressure monitoring.[4] In this artificial eye model (Fig. 16e and f), a spherical polymer shell filled with a hydrogel core served as a deformable sensor for intraocular-pressure monitoring, where mechanical stress within the soft

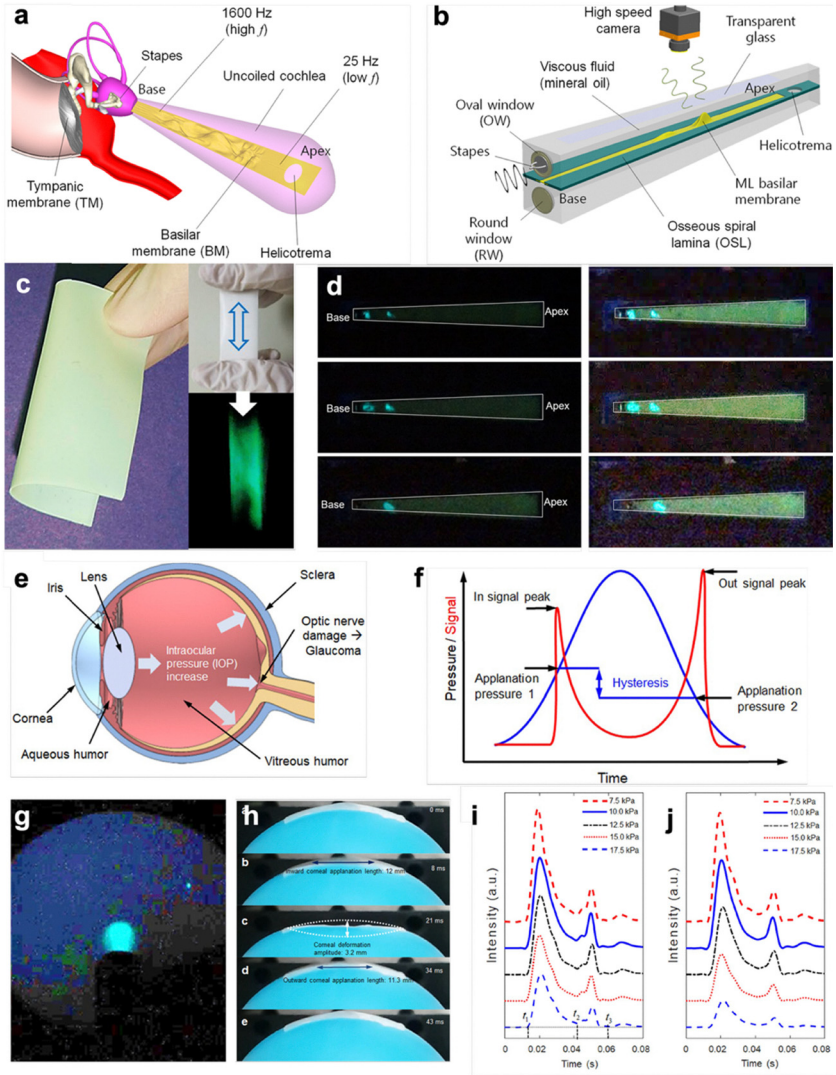

Fig. 16 (a) Schematic of the uncoiled cochlea showing the frequency selectivity of different basilar membrane regions. (b) Conceptual illustration of an artificial cochlea constructed from a mechanoluminescent (ML) basilar membrane. (c) and (d) Optical and pseudocolor ML images captured under cyclic mechanical loading (5 N, 10 mm s^{-1}), demonstrating frequency-dependent luminescence responses at 40–110 Hz. (e) Cross-sectional anatomy of the human eye illustrating intraocular pressure measurement principles. (f) Schematic of a corneal hysteresis-based tonometry setup comparing applanation signal and air pressure over time. (g) Experimental configuration for monitoring internal pressure in a hydrogel-filled spherical polymer shell, with corresponding ML images captured by a high-speed camera (exposure = 30 s). (h) Sequential ML images of corneal deformation in response to air puff stimulation: pre-deformation, inward applanation, maximum concavity, outward applanation, and recovery. (i) and (j) ML intensity profiles at various internal pressures (7.5–17.5 kPa) for ML soft composites with different thicknesses (0.2 mm and 0.6 mm), showing sensitivity dependence on film geometry. (a)–(d) Adapted from Scientific Reports 8, 12023 (2018). (e)–(j) Adapted from Scientific Reports 9, 15215 (2019). Both figures are available under a CC BY 4.0 license. © The Authors.

composite generated measurable luminescence whose intensity correlated with applied pressure (Fig. 16g–j). These examples clearly illustrate that elastomeric polymer matrices not only provide the mechanical compliance and flexibility required for intimate contact with curved biological tissues but also maintain stable emission and optical sensitivity under repeated deformation, thereby enabling the development of noninvasive, bio-mimetic ML platforms for physiological monitoring and sensory replacement.

As part of these advancements, a highly intriguing and distinctive form of sono-optogenetics has been developed, leveraging the ultrasound-responsive characteristics of ML platforms.[43,57,58] Recently, Hong *et al.* developed a comprehensive noninvasive light-delivery strategy termed deLight, which employs circulation-delivered ML nanotransducers (MLNTs, shown in Fig. 17b) to generate localized emission in deep-seated tissue upon focused ultrasound irradiation (Fig. 17a). The MLNTs were dispersed in PDMS phantoms and artificial circulatory systems to mimic biological conditions, demonstrating robust photo-mechanical conversion and minimal cytotoxicity.[59–61] In particular, PDMS served not only as an ultrasound-transmissive medium but also as a biocompatible elastic barrier that protected cells from acoustic shock and nanoparticle aggregation (Fig. 17b and c). This approach enabled the activation of channelrhodopsin-2 (ChR2)-expressing neurons in living mice without craniotomy or optical fiber implantation, demonstrating deep-brain optogenetic control *via* mechanically triggered light emission (Fig. 17d–f).[2,62,63]

Following these innovations, extensive research has been conducted to further enhance the performance and practical applicability of ML materials. Wang *et al.* demonstrated a controllable doping strategy for tunable and multimodal emission in ZnS-based ML nanocrystals. By embedding the phosphors in an elastomeric polymer network similar to Ecoflex, they achieved both mechanical flexibility and enhanced optical efficiency. This architecture allowed multi-color ML responses under varying ultrasound frequencies and pressures, providing a tunable tool for deep-tissue photoactivation and therapeutic biomodulation. Such polymer-encapsulated ML nanocrystals illustrate how elastomeric matrices not only preserve particle functionality *in vivo* but also enhance long-term biostability and reduce immune response.

Taken together, these studies underscore that elastomeric polymers play a dual role in biomedical ML platforms: they facilitate efficient ultrasound transmission to phosphors and simultaneously serve as protective, biocompatible buffers that mitigate mechanical and chemical stress on tissues. Such

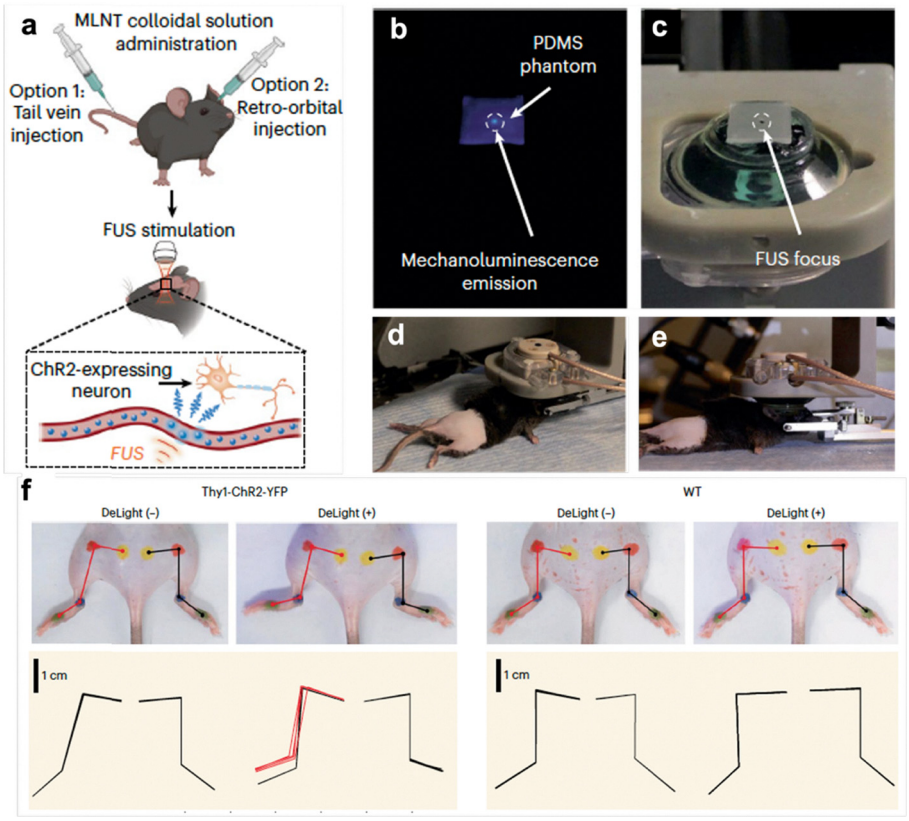

Fig. 17 (a) Schematic illustration of *in vivo* applications of the deLight system. (b) PDMS phantom showing bright ML emission at the ultrasound focus. (c) Marked target point on the PDMS phantom indicating the focal position of the focused ultrasound (FUS) transducer. (d) Sequential movement and positioning of the FUS transducer to the desired brain coordinates. (e) Side-view configuration of the transducer and mouse head, showing spatial alignment during *in vivo* operation. (f) Tracking of mouse limb motion induced by optogenetic neuromodulation *via* deLight-mediated ML in the brain. Adapted from *Nature Protocols* 18, 3787–3820 (2023), © The Authors, distributed under CC BY 4.0.

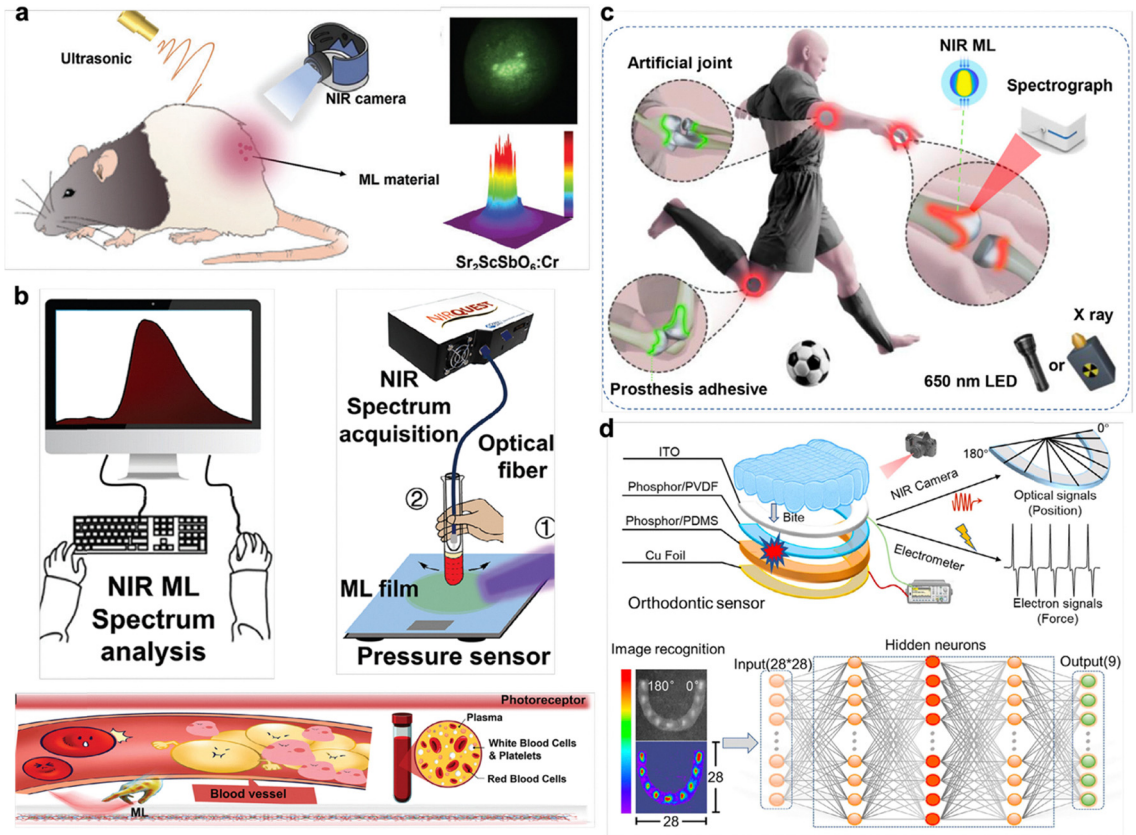

Fig. 18 (a) Ultrasound-triggered NIR ML emission *in vivo* and corresponding 3D mapping of ML films, demonstrating deep-tissue mechanoluminescence activation. Reproduced with permission from Dou *et al.*, *Adv. Funct. Mater.*, © 2024 Wiley-VCH GmbH. (b) Concept of non-destructive NIR ML sensing for metabolic analysis, where defect-engineered NIR ML materials enable optical detection of blood glucose and lipids through biological media. Adapted with permission from Huang *et al.*, *Adv. Sci.*, © 2024 Wiley-VCH GmbH. (c) NIR ML–based stress detection strategy for joint-replacement environments, illustrating how pre-charged ML composites can be read through multilayer tissue for *in-situ* mechanical monitoring. Adapted with permission from Li *et al.*, *Adv. Mater.*, © 2025 Wiley-VCH GmbH. (d) Orthodontic ML appliance integrating NIR ML emission and electrical readout for mapping occlusal forces, bite positions, and micro-strain distributions with high precision. Adapted with permission from Xu *et al.*, *Adv. Mater.*, © 2025 Wiley-VCH GmbH.

polymer-assisted ML systems open a pathway toward noninvasive, safe, and repeatable light-mediated neuromodulation, bridging mechanical energy conversion with next-generation bioelectronic and optogenetic therapies.

Beyond ultrasound-driven ML technologies, recent advances in near-infrared (NIR) ML systems have further expanded the biomedical applicability of polymer-integrated ML platforms. NIR-emitting phosphors, whether based on Cr^{3+}-activated antimonate double perovskites[64] or defect-engineered $YAlO_3$:Cr^{3+} structures,[65] have been embedded within soft elastomeric polymers such as PDMS to form flexible, biocompatible ML composites suitable for operation inside or in direct contact with biological tissues (Fig. 18a and b).

These polymer-supported NIR ML composites enable a new class of noninvasive biomechanical sensing capabilities, including (i) *in situ* stress detection in joint-replacement environments (Fig. 18c), where NIR ML signals can be read through multilayer biological tissue after X-ray or optical pre-charging,[66] and (ii) multilayer orthodontic appliances capable of mapping occlusal forces, bite positions, and micro-strain distributions with clinically relevant resolution (Fig. 18d).[67]

These emerging applications highlight that progress in NIR ML requires not only the development of advanced NIR phosphors[68] but also the refinement of polymer integration strategies, as soft elastomeric matrices play a critical role in maintaining mechanical conformity, stabilizing interfacial charge transfer, and preserving ML emission under physiological deformation. Fig. 18 summarizes these emerging NIR-enabled biomedical ML technologies and highlights how polymer integration continues to propel ML platforms toward next-generation diagnostic, monitoring, and human–machine interfacing applications.

Conclusion

The integration of polymer matrices has fundamentally reshaped the framework of ML, transforming it from a purely stress-driven phenomenon into a mechanically adaptive, field-modulated luminescent platform. By enabling interfacial triboelectric coupling and controlled elastic deformation, polymers actively regulate charge transport, trapping–detrapping dynamics, and overall emission efficiency, thereby improving

brightness, reproducibility, and mechanical adaptability under low mechanical stimuli. These advantages become particularly important when ML platforms are applied to real environments, such as haptic interfaces, healthcare motion monitoring, and deep-tissue or intraoral biomedical systems, where conformal contact, flexibility, and operational stability are essential.

Our summaries also underscore that polymer selection cannot be universal or empirical. Effective integration must begin with a clear understanding of the intrinsic ML mechanisms of the chosen phosphor. Only when phosphors with the appropriate defect structures, carrier dynamics, or piezo–triboelectric response characteristics are identified can polymer matrices contribute meaningfully to interfacial field generation and emission modulation. Based on these considerations, we outlined three core criteria for polymer selection: optical transparency to preserve photon output, mechanical elasticity to enable controlled gap formation at the interface, and triboelectric polarity to maximize charge density. These principles form a mechanism-guided framework for choosing suitable polymers across different ML systems.

Looking ahead, progress in ML will increasingly rely on the co-design of phosphors and polymers rather than treating them as independent components. Future studies should identify phosphors whose luminescence mechanisms inherently complement polymer-mediated triboelectric effects, while concurrently developing polymers with tailored dielectric constants, elastic moduli, and triboelectric signatures that optimally couple with these ML behaviors. Quantitative correlations between polymer physicochemical properties and ML emission characteristics will be crucial for predictive materials screening. Additionally, multi-phase elastomers, gradient or porous architectures, and hybrid tribo–piezoelectric matrices offer promising routes to fine-tune interfacial field strength and mechanical compliance.

Ultimately, the convergence of mechanism-guided phosphor selection and rational polymer design is expected to drive the next generation of ML platforms. By bridging fundamental materials chemistry with functional device engineering, this integrated design approach will accelerate the development of scalable, durable, and energy-autonomous ML technologies for advanced sensing, diagnostics, and biomedical systems.

Conflicts of interest

There are no conflicts to declare.

Data availability

Data sharing is not applicable to this article as no datasets are generated or analysed during the current study.

Acknowledgements

S. B. acknowledges financial support from the Basic Science Research Program through the National Research Foundation of Korea (NRF), funded by the Ministry of Education, under the Brain Pool Fellowship (RS-2023-00263849). This work was supported by National Research Foundation of Korea (NRF-2022R1A2C1002764 and RS-2025-25402595). H. C. acknowledges the Korea Basic Science Institute (National Research Facilities and Equipment Center) grant funded by the Ministry of Education (2022R1A6C101A779).

References

1 Y. Zhuang and R. Xie, Mechanoluminescence Rebrightening the Prospects of Stress Sensing: A Review, *Adv. Mater.*, 2021, **33**, 2005925.
2 X. Wu, X. Zhu, P. Chong, J. Liu, L. N. Andre, K. S. Ong, K. Brinson, A. I. Mahdi, J. Li, L. E. Fenno, H. Wang and G. Hong, Sono-optogenetics facilitated by a circulation-delivered rechargeable light source for minimally invasive optogenetics, *Proc. Natl. Acad. Sci. U. S. A.*, 2019, **116**, 26332–26342.
3 D. Zhou, Z. Zhang, B. Qiu, D. Zhang, S. Xie, K. Huang and X. Li, Ultrasound-Activated Persistent Luminescence Imaging and Bacteria-Triggered Drug Release for *Helicobacter pylori* Infection Theranostics, *ACS Appl. Mater. Interfaces*, 2022, **14**, 26418–26430.
4 Y. Kim, S. Roy, G.-Y. Jung, J.-S. Oh and G.-W. Kim, Dual Optical Signal-based Intraocular Pressure-sensing Principle Using Pressure-sensitive Mechanoluminescent ZnS:Cu/PDMS Soft Composite, *Sci. Rep.*, 2019, **9**, 15215.
5 H. I. Jeong, H. S. Jung, M. Dubajic, G. Kim, W. H. Jeong, H. Song, Y. Lee, S. Biswas, H. Kim, B. R. Lee, J. W. Yoon, S. D. Stranks, S. M. Jeong, J. Lee and H. Choi, Super elastic and negative triboelectric polymer matrix for high performance mechanoluminescent platforms, *Nat. Commun.*, 2025, **16**, 854.
6 C. Li, Q. He, Y. Wang, Z. Wang, Z. Wang, R. Annapooranan, M. I. Latz and S. Cai, Highly robust and soft biohybrid mechanoluminescence for optical signaling and illumination, *Nat. Commun.*, 2022, **13**, 3914.
7 J. Xiao, Y. Cai, Y. Song, H. Tang, P. Zhang, Q. Peng, X. Xu, Z. Liu and L. Zhao, High Stable Mechanoluminescence from $TbBO_3$ GCs for Stress Safety Monitoring, *Laser Photonics Rev.*, 2024, **18**, 2301002.
8 C. Li, N. Schramma, Z. Wang, N. F. Qari, M. Jalaal, M. I. Latz and S. Cai, Ultrasensitive and robust mechanoluminescent living composites, *Sci. Adv.*, 2023, **9**, eadi8643.
9 S. F. Bacon, The Online Library of Liberty.
10 A. Feng and P. F. Smet, A Review of Mechanoluminescence in Inorganic Solids: Compounds, Mechanisms, Models and Applications, *Materials*, 2018, **11**, 484.
11 J. Yu, Q. Niu, Y. Liu, Y. Bu, H. Zou and X. Wang, Principles, properties, and sensing applications of mechanoluminescence materials, *J. Mater. Chem. C*, 2023, **11**, 14968–15000.
12 J.-C. Zhang, C.-N. Xu, S. Kamimura, Y. Terasawa, H. Yamada and X. Wang, An intense elastico-mechanoluminescence material CaZnOS:Mn^2+ for sensing and imaging multiple mechanical stresses, *Opt. Express*, 2013, **21**, 12976.

13 M. R. Rahimi, G. J. Yun, G. L. Doll and J.-S. Choi, Effects of persistent luminescence decay on mechanoluminescence phenomena of SrAl_2O_4:Eu2+, Dy3+ materials, *Opt. Lett.*, 2013, **38**, 4134.
14 Y. Wang, X. Zhang, B. Ren, J. Zhang, Q. Zhang, Z. Fang, M. Wu, L. Li, Y. Yang, Y. Zhuang, G. Bai, J. Gan and D. Peng, Smart Semiconductors: An Overview of AZnOS (A= Ca, Sr, Ba) Based Phosphors, Multi-Stimuli Responsive Luminescence, and Potential Application Prospects, *Adv. Sci.*, 2025, e13923.
15 V. K. Chandra, B. P. Chandra and P. Jha, Self-recovery of mechanoluminescence in ZnS:Cu and ZnS:Mn phosphors by trapping of drifting charge carriers, *Appl. Phys. Lett.*, 2013, **103**, 161113.
16 Z. Huang, X. Li, T. Liang, B. Ren, X. Zhang, Y. Zheng, Q. Zhang, Z. Fang, M. Wu, M. Zulfiqar, L. Jing, S. Qu, B. Chen, J. Gan and D. Peng, Smart mechanoluminescent phosphors: A review of zinc sulfide-based materials for advanced mechano-optical applications, *Responsive Mater.*, 2024, **2**, e20240019.
17 J.-C. G. Bünzli and K.-L. Wong, Lanthanide mechanoluminescence, *J. Rare Earths*, 2018, **36**, 1–41.
18 S. Moon Jeong, S. Song, S.-K. Lee and B. Choi, Mechanically driven light-generator with high durability, *Appl. Phys. Lett.*, 2013, **102**, 051110.
19 H.-J. Park, S. Kim, J. H. Lee, H. T. Kim, W. Seung, Y. Son, T. Y. Kim, U. Khan, N.-M. Park and S.-W. Kim, Self-Powered Motion-Driven Triboelectric Electroluminescence Textile System, *ACS Appl. Mater. Interfaces*, 2019, **11**, 5200–5207.
20 X. Wang, D. Peng, B. Huang, C. Pan and Z. L. Wang, Piezophotonic effect based on mechanoluminescent materials for advanced flexible optoelectronic applications, *Nano Energy*, 2019, **55**, 389–400.
21 H. I. Jeong, H. S. Jung, C. B. Lee, S. J. Kim, J.-S. Jo, S. Song, S.-J. Ko, D.-W. Kang, S. M. Jeong, J.-W. Jang, K. Kim, J. Lee and H. Choi, Interfacial dipole moment engineering in self-recoverable mechanoluminescent platform, *Mater. Today*, 2024, **81**, 4–11.
22 G. Lee, S. Song, W. H. Jeong, C. Lee, J. Kim, J. Lee, J. Choi, H. Choi, Y. Kim, S. J. Lim and S. M. Jeong, Interfacial Triboelectricity Lights Up Phosphor-Polymer Elastic Composites: Unraveling the Mechanism of Mechanoluminescence in Zinc Sulfide Microparticle-Embedded Polydimethylsiloxane Films, *Small*, 2024, 2307089.
23 S. Chang, K. Zhang, D. Peng, Y. Deng, C.-X. Shan and L. Dong, Mechanoluminescent functional devices: Developments, applications and prospects, *Nano Energy*, 2024, **122**, 109325.
24 H. Zhang, Y. Wei, X. Huang and W. Huang, Recent development of elastico-mechanoluminescent phosphors, *J. Lumin.*, 2019, **207**, 137–148.
25 L. Jiang, Y. Du, X. Zhang, N. Ma, X. Liu and A. S. Abd-El-Aziz, A Review of Mechanoluminescence Based on Quaternary Oxysulfides: Research Progress, Mechanism and Applications, *J. Inorg. Organomet. Polym.*, 2024, **34**, 3008–3027.
26 A. Qasem, P. Xiong, Z. Ma, M. Peng and Z. Yang, Recent Advances in Mechanoluminescence of Doped Zinc Sulfides, *Laser Photonics Rev.*, 2021, **15**, 2100276.
27 J.-C. Zhang, X. Wang, G. Marriott and C.-N. Xu, Trap-controlled mechanoluminescent materials, *Prog. Mater. Sci.*, 2019, **103**, 678–742.
28 S. M. Jeong, S. Song, S.-K. Lee and N. Y. Ha, Color Manipulation of Mechanoluminescence from Stress-Activated Composite Films, *Adv. Mater.*, 2013, **25**, 6194–6200.
29 R. S. Fontenot and W. A. Hollerman, Measuring triboluminescence from ZnS:Mn produced by ballistic impacts, *J. Inst.*, 2011, **6**, T04001.
30 L. Kobakhidze, C. J. Guidry, W. A. Hollerman and R. S. Fontenot, Detecting Mechanoluminescence From ZnS:Mn Powder Using a High Speed Camera, *IEEE Sens. J.*, 2013, **13**, 3053–3059.
31 M. V. Mukhina, J. Tresback, J. C. Ondry, A. Akey, A. P. Alivisatos and N. Kleckner, Single-Particle Studies Reveal a Nanoscale Mechanism for Elastic, Bright, and Repeatable ZnS:Mn Mechanoluminescence in a Low-Pressure Regime, *ACS Nano*, 2021, **15**, 4115–4133.
32 H. I. Jeong, M. Dubajic, C. B. Lee, S.-J. Woo, X. W. Chua, T. Kang, Y. Han, J. Yang, J. Lee, S.-J. Ko, D.-W. Kang, K. Kim, S. D. Stranks and H. Choi, Defect Localized Mechanoluminescence Model in Copper Doped Zinc Sulfide, *ACS Nano*, 2025, **19**, 35027–35036.
33 B. Chen, X. Zhang and F. Wang, Expanding the Toolbox of Inorganic Mechanoluminescence Materials, *Acc. Mater. Res.*, 2021, **2**, 364–373.
34 T. Richhariya, N. Brahme, D. P. Bisen, Y. Patle, E. Chandrawanshi and N. Shah, Luminescence properties of blue-emitting Ce3 + -doped series of Ca2Al2SiO7 and Sr2Al2SiO7 phosphors, *J. Mater. Sci.: Mater. Electron.*, 2021, **32**, 20793–20803.
35 Z. Monette, A. K. Kasar and P. L. Menezes, Advances in triboluminescence and mechanoluminescence, *J. Mater. Sci.: Mater. Electron.*, 2019, **30**, 19675–19690.
36 R. Ma, X. Wei, C. Wang, S. Mao, B. Chen, Y. Shao, Y. Fu, K. Yan and D. Peng, Reproducible mechanical-to-optical energy conversion in Mn (II) doped sphalerite ZnS, *J. Lumin.*, 2021, **232**, 117838.
37 C.-N. Xu, T. Watanabe, M. Akiyama and X.-G. Zheng, Direct view of stress distribution in solid by mechanoluminescence, *Appl. Phys. Lett.*, 1999, **74**, 2414–2416.
38 H. Yamada, X. Fu and C.-N. Xu, Enhancement of Adhesion and Triboluminescent Properties of SrAl2O4:Eu2+ Films Fabricated by RF Magnetron Sputtering and Postannealing Techniques, *J. Electrochem. Soc.*, 2007, DOI: 10.1149/1.2772194.
39 J.-C. Zhang, C.-N. Xu and Y.-Z. Long, Elastico-mechanoluminescence in CaZr(PO_4)_2:Eu^2+ with multiple trap levels, *Opt. Express*, 2013, **21**, 13699.
40 B. Huang, Energy harvesting and conversion mechanisms for intrinsic upconverted mechano-persistent luminescence in CaZnOS, *Phys. Chem. Chem. Phys.*, 2016, **18**, 25946–25974.
41 M.-C. Wong, L. Chen, G. Bai, L.-B. Huang and J. Hao, Temporal and Remote Tuning of Piezophotonic-Effect-

Induced Luminescence and Color Gamut via Modulating Magnetic Field, *Adv. Mater.*, 2017, **29**, 1701945.
42 J. S. Kim and G.-W. Kim, New non-contacting torque sensor based on the mechanoluminescence of ZnS:Cu microparticles, *Sens. Actuators, A*, 2014, **218**, 125–131.
43 Z. Wang, L. Jin, H. Ni, H. Kim, Y. Zeng, Q. Zhou, M. Chi, J. Nam and Y. Yin, Controllable Doping for Tunable and Multimodal Emission in ZnS-Based Mechanoluminescent Nanocrystals, *Nano Lett.*, 2025, **25**, 11747–11755.
44 B. P. Chandra, V. K. Chandra, P. Jha and V. D. Sonwane, Threshold pressure for mechanoluminescence of macrocrystals, microcrystals and nanocrystals of doped zinc sulphide, *Phys. B*, 2016, **491**, 12–16.
45 X. Qian, Z. Cai, M. Su, F. Li, W. Fang, Y. Li, X. Zhou, Q. Li, X. Feng, W. Li, X. Hu, X. Wang, C. Pan and Y. Song, Printable Skin-Driven Mechanoluminescence Devices via Nanodoped Matrix Modification, *Adv. Mater.*, 2018, **30**, 1800291.
46 W. Wang, Z. Wang, J. Zhang, J. Zhou, W. Dong and Y. Wang, Contact electrification induced mechanoluminescence, *Nano Energy*, 2022, **94**, 106920.
47 W. Wang, Z. Li, Z. Wang, Z. Xiang, Z. Wang, S. Li, M. Zhang and W. Liu, Achieving Tunable Mechanoluminescence in CaZnOS:Tb3 +, Sm3+ for Multicolor Stress Sensing, *Nanomaterials*, 2024, **14**, 1279.
48 J. Botterman, K. V. D. Eeckhout, I. D. Baere, D. Poelman and P. F. Smet, Mechanoluminescence in BaSi2O2N2:Eu, *Acta Mater.*, 2012, **60**, 5494–5500.
49 W. Wang, S. Wang, Y. Gu, J. Zhou and J. Zhang, Contact-separation-induced self-recoverable mechanoluminescence of CaF2:Tb3 +/PDMS elastomer.
50 T. Wang, P. Zhang, J. Xiao, Z. Guo, X. Xie, J. Huang, J. Zheng, X. Xu and L. Zhao, Trap Assisted Dynamic Mechanoluminescence Toward Self-Referencing and Visualized Strain Sensing, *Adv. Sci.*, 2025, **12**, 2410673.
51 H. J. Kim, S. Ji, J. Y. Han, H. B. Cho, Y.-G. Park, D. Choi, H. Cho, J.-U. Park and W. B. Im, Detection of cracked teeth using a mechanoluminescence phosphor with a stretchable photodetector array, *NPG Asia Mater.*, 2022, **14**, 26.
52 B. Hou, L. Yi, C. Li, H. Zhao, R. Zhang, B. Zhou and X. Liu, An interactive mouthguard based on mechanoluminescence-powered optical fibre sensors for bite-controlled device operation, *Nat. Electron.*, 2022, **5**, 682–693.
53 H. I. Jeong, S. E. Choi, X. W. Chua, N. W. Kim, E. Pyrilli, H. Lee, D. Kang, B. R. Lee, S. D. Stranks, J. Kim, S. Bandyopadhyay and H. Choi, High-Resolution Mechanoluminescent Haptic Sensor via Dual-Functional Chromatic Filtration by a Conjugated Polymer Shell, *Adv. Mater.*, 2025, e08917.
54 B. Zhou, J. Liu, X. Huang, X. Qiu, X. Yang, H. Shao, C. Tang and X. Zhang, Mechanoluminescent-Triboelectric Bimodal Sensors for Self-Powered Sensing and Intelligent Control, *Nano-Micro Lett.*, 2023, **15**, 72.
55 M. Yang, X. Ge, L. Zheng, Y. Huang, J. Zhong, D. Tu, G. Hong and F. Yang, Mechanoluminescent Light Sources Based on Nanostructured Systems for Biomedical Applications: A Review, *ACS Appl. Nano Mater.*, 2024, **7**, 26515–26533.
56 Y. Kim, J.-S. Kim and G.-W. Kim, A Novel Frequency Selectivity Approach Based on Travelling Wave Propagation in Mechanoluminescence Basilar Membrane for Artificial Cochlea, *Sci. Rep.*, 2018, **8**, 12023.
57 S. Jiang, X. Wu, F. Yang, N. J. Rommelfanger and G. Hong, Activation of mechanoluminescent nanotransducers by focused ultrasound enables light delivery to deep-seated tissue in vivo, *Nat. Protoc.*, 2023, **18**, 3787–3820.
58 Z. Wang, L. Jin, E. Tiukalova, Y. Tai, Y. Zeng, D. Kim, Q. Zhou, M. Chi, J. Nam and Y. Yin, Size and Structural Control of Mechanoluminescent ZnS:Mn^{2+} Nanocrystals for Optogenetic Neuromodulation, *ACS Nano*, 2025, **19**, 19340–19352.
59 F. Yang, X. Wu, H. Cui, S. Jiang, Z. Ou, S. Cai and G. Hong, Palette of Rechargeable Mechanoluminescent Fluids Produced by a Biomineral-Inspired Suppressed Dissolution Approach, *J. Am. Chem. Soc.*, 2022, **144**, 18406–18418.
60 F. Yang, X. Wu, H. Cui, Z. Ou, S. Jiang, S. Cai, Q. Zhou, B. G. Wong, H. Huang and G. Hong, A biomineral-inspired approach of synthesizing colloidal persistent phosphors as a multicolor, intravital light source, *Sci. Adv.*, 2022, **8**, eabo6743.
61 F. Yang, S.-J. Kim, X. Wu, H. Cui, S. K. Hahn and G. Hong, Principles and applications of sono-optogenetics, *Adv. Drug Delivery Rev.*, 2023, **194**, 114711.
62 G. Hong, Seeing the sound, *Science*, 2020, **369**, 638.
63 W. Wang, X. Wu, K. W. Kevin Tang, I. Pyatnitskiy, R. Taniguchi, P. Lin, R. Zhou, S. L. C. Capocyan, G. Hong and H. Wang, Ultrasound-Triggered In Situ Photon Emission for Noninvasive Optogenetics, *J. Am. Chem. Soc.*, 2023, **145**, 1097–1107.
64 C. Dou, T. Liang, M. Zhao, Z. Song, L. Ning, D. Peng and Q. Liu, Self-Recoverable and NIR-I to NIR-II Tunable Broadband Mechanoluminescence of Cr3+ -Doped Antimonate Double Perovskites, *Adv. Funct. Mater.*, 2025, **35**, 2419716.
65 S. Wu, G. Zhou, Y. Wu, P. Xiong, B. Xiao, Z. Zhou, Y. Xiao, P. Shao, S. Wang, Z. Shao, Y. Wang and F. Wang, Multiple Defect-Induced High-Resolution Near-Infrared Mechanoluminescent Materials for Non-Destructive Detection of Blood Glucose and Lipids, *Adv. Mater.*, 2024, **36**, 2408508.
66 W. Li, P. Xiong, X. Zheng, L. Niu, L. Cui, Q. Wang, B. Viana, P. Dorenbos, J. Zhang and J. Ren, Micro-Strain Responsive Near-Infrared Mechanoluminescence for Potential Nondestructive Artificial Joint Stress Imaging, *Adv. Mater.*, 2025, e05360.
67 S. Xu, Y. Xiao, P. Xiong, P. Zheng, S. Wu, X. Wang, Y. Yin, H. Fang, C. Wang, Y. Lu, E. Song and J. Gan, Boosting Mechanoluminescence Performance in Doped CaZnOS by the Facile Self-Reduction Approach, *Adv. Mater.*, 2025, e11643.
68 S. Wu, S. Wang, Z. Shao, Y. Wang and P. Xiong, Self-powered near-infrared mechanoluminescence through MgO/MgF2 piezo-photonic heterojunctions, *Nat. Commun.*, 2025, **16**, 8912.

